University of Kentucky

UKnowledge

University of Kentucky Doctoral Dissertations   Graduate School

2003

MODELING THE INFRARED EMISSION FROM DUST IN ACTIVE GALACTIC NUCLEI

Maia M. Nenkova
University of Kentucky, maia@pa.uky.edu

Right click to open a feedback form in a new tab to let us know how this document benefits you.

ABSTRACT OF DISSERTATION

Maia M. Nenkova

The Graduate School

University of Kentucky

2003

MODELING THE INFRARED EMISSION
FROM DUST IN ACTIVE GALACTIC NUCLEI

ABSTRACT OF DISSERTATION

A dissertation submitted in partial fulfillment of the
requirements for the degree of Doctor of Philosophy
in the College of Arts and Sciences at the University of Kentucky

By

Maia M. Nenkova

Lexington, Kentucky

Director: Dr. Moshe Elitzur, Professor of Physics and Astronomy

Lexington, Kentucky

2003

ABSTRACT OF DISSERTATION

MODELING THE INFRARED EMISSION
FROM DUST IN ACTIVE GALACTIC NUCLEI

Active Galactic Nuclei (AGN) are compact regions in the centers of some galaxies. They emit significantly in the whole range of the electromagnetic spectrum and show variability at different timescales. Observational evidence suggests the presence of a dusty torus obscuring the central radiation source of AGN. According to the Unified Model the observed general properties of AGN emission can be understood on the basis of orientation of this torus toward an observer. Two main types of AGN are distinguished: Type 1, with detected emission from the inner torus cavity viewed pole-on, and Type 2, viewed through the obscuring torus.

There are numerous attempts in the past decade to model the emission from the torus, considering a homogeneous distribution of dust. However, important problems in explaining the observations still remain unsolved: it is hard to suppress the 10 μm emission feature of silicate dust for a pole-on view and at the same time produce an absorption feature for an edge-on viewed torus; despite the huge optical depths inferred from X-ray observations of Type 2 sources, the observed absorption feature is shallow. Unlike observations, models of homogeneous

tori with large optical depths always produce deep absorption feature. While it is realized that dust contained in clumps would resolve these issues, modeling of a clumpy medium poses a serious computational challenge.

We are the first to incorporate clumps in our model of a dusty torus and to successfully explain the infrared emission from AGN. We model two types of clouds: directly illuminated by the AGN and diffusely heated by other clouds. We calculate the emission of the first type as angle-averaged emission from a dusty slab. The second type of clouds is modeled as dusty spheres embedded in the radiation field of the directly heated clouds. The radiative transfer problem for a dusty slab and externally heated sphere is solved exactly with our code DUSTY. The overall emission of the torus is found by integration over the spatial distribution of clouds. We find a very good agreement of our model results with observations. Comparison with them can constrain the physical conditions in the AGN dusty tori.

KEYWORDS: Active Galactic Nuclei, AGN torus, Clumpy Torus, Clumps, Dust Emission, Radiative Transfer, Infrared

Maia Nenkova

May 8, 2003

MODELING THE INFRARED EMISSION
FROM DUST IN ACTIVE GALACTIC NUCLEI

By

Maia M. Nenkova

Dr. Moshe Elitzur
(Director of Dissertation)

Dr. Thomas Troland
(Director of Graduate Studies)

May 8, 2003
(Date)

RULES FOR THE USE OF DISSERTATIONS

DISSERTATION

Maia M. Nenkova

The Graduate School

University of Kentucky

2003

MODELING THE INFRARED EMISSION
FROM DUST IN ACTIVE GALACTIC NUCLEI

DISSERTATION

A dissertation submitted in partial fulfillment of the
requirements for the degree of Doctor of Philosophy
in the College of Arts and Sciences at The University of Kentucky

By

Maia M. Nenkova

Lexington, Kentucky

Director: Dr. Moshe Elitzur, Professor of Physics and Astronomy

Lexington, Kentucky

2003

To my parents

Acknowledgments

I would not have reached this moment of my life and this work would not have been completed without the constant support and encouragement of my advisor, Moshe Elitzur. Throughout the years he kept leading me in the right direction in the painful process of discovering Nature's inner workings, providing his invaluable insight in moments of doubt. I admire his innate drive toward perfection, his strife for finding the ultimate truths. I am deeply indebted to him for all the good qualities that he taught me of, and for showing me what a real teacher should be.

Thanks to my other teachers at the Dept. of Physics and Astronomy, Isaac Shlosman and Keith MacAdam who expanded my horizons, and supported me through all these years, to Tom Troland, who, as DGS, was always helpful in administrative and other matters. My deep thanks and appreciation to the members of my committee, M. Pinar Mengüç and Laurence Hassebrook, for their time and willingness to referee this work. Thanks also to John Connoly, the Director of the CCS at UK, for granting a 3 year fellowship which allowed me to devote more time to research.

I am especially grateful to Željko Ivezić for his help and advice whenever I needed it. My warm thanks to Almudena Alonso-Herrero and Nancy Levenson for our fruitful discussions and collaboration. Thanks also to all other friends and colleagues, for being with me in times of struggle and joy.

And last, but not least, my deep gratitude to my husband Constantine and children Yavor and Kalin, for all their patience, love and support through the years. I am especially thankful to my parents, who taught me to never give up and always encouraged me to follow my interests. Without all these people in my life I would not be what I am today.

Table of Contents

List of Figures

Chapter 1

Introduction

1.1   Active Galactic Nuclei

Active Galactic Nuclei (AGN) are peculiar and fascinating objects in the Universe, residing in the central regions of some galaxies. Observations indicate that they are very compact, emit significantly in the whole range of the electromagnetic spectrum and show variability at different timescales, from hours and days, to months. AGN have enormous energy outputs: with luminosities of the order of, typically 10^{10}- $10^{13} L_{\odot}$ and higher, they are the most energetic objects known.

Historically, the Seyfert Galaxies were discovered first at the lower end of the luminosity range, showing unusually broad emission lines in their spectra. With the advancement of observational techniques a wealth of new data accumulated, adding more pieces to the puzzle of the nature of AGN. Radio galaxies with excessive radio emission and prominent jets from their nuclei, as well as quasars (quasi-stellar radio sources) were discovered as objects occupying the higher end of the luminosity range. As a result, it was initially thought that they were separate classes of objects.

Numerous studies in the last two decades indicate that all AGN, from Seyfert nuclei to quasars, appear to belong to one family (see e.g., Osterbrock 1993 and references therein). This means they must have a similar physical nature and a similar powerful energy source. All models of AGN suggest the existence of a supermassive (10^6- $10^9 M_{\odot}$) black hole which develops at the center of the galaxy. Gas, in-falling in this massive black hole, forms an accretion disk, emitting high-

energy radiation. The black hole and accretion disk are the so called central engine, the radiation source powering the AGN.

The nuclei of Seyfert galaxies are the AGN, that are nearest to us, and according to Osterbrock & Martel (1993) they are about 1% of the nuclei of the luminous spiral galaxies. Two main types were spectroscopically classified: Seyfert 1 (Sy1), with strong broad permitted emission lines and narrow forbidden emission lines, and Seyfert 2 (Sy2), with strong narrow permitted and forbidden emission lines (Osterbrock 1993). Broad lines were also observed in the quasar spectra. The large observed Doppler broadening of the emission lines indicate that the gas in the emitting region (the Broad Line Region, or BLR) must have a large range of internal velocities, resulting from rotation and turbulent motions. The narrow lines must be emitted from regions with lower electron densities compared to the BLR and lower gas velocities (the Narrow Line Region, or NLR).

A more detailed qualification of the Seyferts considers additional intermediate classes: Sy1.5, with strong broad and narrow components of their permitted emission lines; Sy1.8, with strong narrow and weak broad components of permitted Balmer Hydrogen lines, H_α and H_β; and Sy1.9, with a weaker broad component of H_α and H_β too faint to be visible. All Seyfert types appear to form a continuous sequence (Osterbrock & Martel 1993).

Reviews and books about AGN abound (see, e.g., Antonucci 1993, Robson 1996, Peterson 1997, Wills 1999, Krolik 1999, and references therein), which trace the gradual accumulation of observational facts and the emergence of a model of possible AGN morphology.

The first indication that there is dust around AGN came from observations of Seyfert galaxies in the late 1970's. They revealed excess infrared emission at wavelengths longer than $\sim 1 - 2\mu$m, which was recognized as a typical dust signature (see, e.g., Rieke & Low 1975, Rowan-Robinson 1977, Rieke & Lebofski 1981). Cosmic dust consists mainly of silicates and carbonaceous grains, in various proportions and size distributions, depending on the environment. For reference, the dust in our galaxy consists of graphite and silicates with sizes up to about

0.25 μm. Dust scatters and absorbs radiation, heats up and re-emits at longer wavelengths, therefore an observed infrared excess is always a prime indicator of dust.

The typical spectrum of an AGN has a pronounced wide "bump" starting at $\sim 1 - 2$ μm and extending to about 100 μm (Fig.1.1). Barvainis (1987) showed that dust heated by the optical/UV continuum of the AGN provides a natural explanation of the observed IR bump. The temperature corresponding to these wavelengths matched the condensation temperature ($\sim$ 1500K) of typical astronomical dust grains. The estimated dust condensation radius was $\sim 1pc$ for typical AGN luminosities of $10^{12}L_{\odot}$.
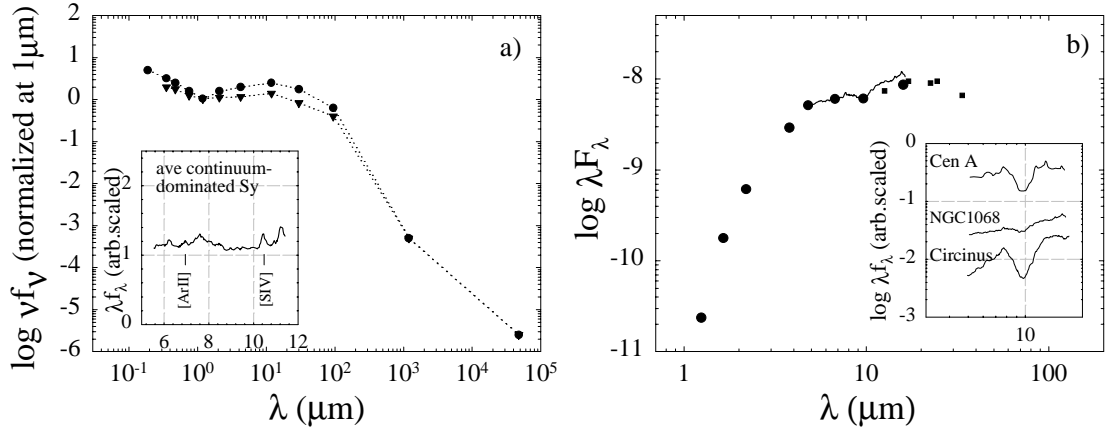
Figure 1.1: Typical spectra of Type 1 (a) and Type 2 (b) AGN. Type 1 is represented by the average spectrum of the 109 PG quasars (Sanders et al 1989). A typical Type 2 source is the Sy2 galaxy NGC1068 (data by Alonso-Herrero et al 2003, LeFloch et al 2001 and Rieke & Low 1975). The inserts show the lack of the silicate emission feature in Type 1 (Spoon et al 2002) and the shallow absorption feature in Type 2 sources (Mirabel et al 1999).

In many Sy2 ionizing photons are observed to escape anisotropically, thus forming ionization cones (Wilson & Tzvetanov 1994). Many sources also show jets of material collimated along these cones. The existence of a collimating anisotropic structure around the AGN, such as a dusty torus, can offer a natural explanation for these observations (Storchi-Bergmann et al 1992).

Antonucci & Miller (1985) discovered that some Sy2 spectra, observed in po-

larized light, show broad lines, which are the characteristics of a Sy1. The degree of polarization was consistent with the assumption that broad line spectra, originating close to the central engine, were reflected or scattered off some medium instead of being directly observed. This gave rise to the idea that Sy2 nuclei contain a Sy1 nucleus in their interiors which is hidden from direct view by an obscuring torus. In other words, the orientation of the torus to an observer would determine the type of source seen.

Strong attenuation of short-wavelength radiation is observed in Type 2 sources, in accordance with the torus model. Measuring the attenuation of hard X-rays $(2-10$ keV$)$ one can estimate the column density of the obscuring torus. Recent results suggest $N_H \sim 10^{22}$- $10^{24} cm^{-2}$ and even higher values for Sy2s (see, e.g., Smith & Done 1996, Bassani et al 1999, and Guainazzi et al 2001).

Direct evidence for the torus existence was obtained by the Hubble Space Telescope (Jaffe et al 1993) and from recent imaging results (Simpson et al 1996, Gallimore et al 1997). Observations of the typical Sy2 galaxy NGC1068, taken at Near-Infrared (NIR) and Mid-Infrared (MIR) wavelengths (Marco & Alloin 2000, Alloin et al 2000 and Bock et al 2000) suggest that the torus most probably extends to a few tens of parsecs from the central engine. Based on the accumu-
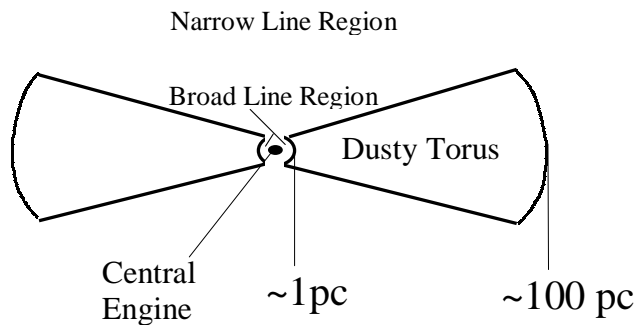
Figure 1.2: A schematic view of the AGN dusty torus with typical scale sizes. An observer looking pole-on would see the broad line region and features of a Type 1 object; an edge-on view would hide the region around the central engine and produce Type 2 features. For reference, 1pc= 3.1×10^{18}cm.

lated observational evidence for existence of a dusty torus the Unification Model gradually emerged. In the frame of the model the two types of AGN are intrinsi-

cally the same objects. The phenomenological differences are result of a different orientation of the obscuring torus toward the observer. Type 1 sources are the predominantly pole-on viewed objects, e.g., most quasars and Sy1 galaxies, while Type 2 are observed edge-on: a few quasars and Sy2 galaxies (for Type 2 quasars see Franceschini et al 2000, Akiyama et al 2002, Norman et al 2002 and Stern et al 2002). Thus, an observer looking at the AGN at small viewing angles (pole-on) will see the emission of the central engine and will observe the broad lines. This would give rise to Type 1 spectrum. An edge-on orientation of the dusty torus toward the observer would hide the central engine and produce a Type 2 spectrum (Fig. 1.2).

Similarly to Seyfert galaxies, radio-galaxies and quasars were also unified, with the former viewed through an obscuring torus and the latter oriented pole-on to an observer.

While imaging, along with the general SED profile of radio-quiet quasars and AGN (Sanders et al 1989, Elvis et al 1994), are evidence for dust thermal emission, higher resolution data in the mid-infrared are needed to constrain the type of dust. Galactic type dust has a typical broad spectral feature at 10μm due to silicates. It can be seen in emission from optically thin heated dust, or in absorption, when colder dust is obscuring a radiation source from an observer.

Aitken & Roche (1985) and Roche et al (1991) obtained narrow aperture $8-13$ μm spectra of 60 AGN, which show that Sy1 and quasars are characterized by a featureless spectrum, while in Sy2 the feature always appears in absorption. Recent spectroscopy results from the Infrared Space Observatory (ISO) confirm that an almost featureless $2.5-11$ μm spectrum is typical for Sy1's and a silicate absorption feature is observed in Sy2's (Clavel et al 2000, Spoon et al 2002). This is a surprising result, since according to the Unified Model the dust should be the same in both types of objects, therefore the silicate feature should be observed either in emission (in Type 1 sources) or in absorption (in Type 2 sources).

1.2 Problems still unsolved by existing models

Explaining the growing volume of observational results made theoretical modeling of the torus a necessity. The problems in modeling the emission from the dusty AGN torus are: i) the observed spectral shape and broad IR emission has to be reproduced correctly; ii) the silicate feature in Type 1 objects has to be suppressed, while at the same time in Type 2 objects a shallow absorption feature has to appear; iii) this shallow silicate absorption feature must be produced despite the enormous optical depths inferred from X-ray observations. As shown by the extensive modeling of quasar and AGN emission described in the literature so far, resolving all issues in a single model can not be easily achieved.

Generally, there are two approaches toward solving the problem with the silicate emission feature: the first is toward modifying dust composition, by reducing the silicate abundance and/or dust size distribution (considering large dust grains). The other approach is to model the transfer of radiation in anisotropic distributions of standard dust, trying to find distribution parameters that would satisfy the observational constrains.

Among studies in direction of the first approach is the comprehensive search in the parameter space of dust size distribution and chemical composition by Laor & Draine (1993). Employing models with spherical and planar geometry they concluded that the 10μm silicate feature can be suppressed only by a significant depletion of silicates and/or presence of very large (up to 10μm) grains. Loska et al (1993) modified a spherical dust distribution around the source by introducing inner cavities devoid of silicates. Silicates are one of the two major dust constituents in our Galaxy (Draine & Lee 1984) and having dust composition preferentially depleted from silicates in the AGN dusty tori seems unlikely. Furthermore, this is not in accordance with the unification models, since depletion of silicates has to be assumed for Sy1 only and not for dust in Sy2.

The other line of studies is exact calculation of radiative transfer in toroidal configurations of continuous dust distribution around the central engine. Pier & Krolik (1992) and Pier & Krolik (1993) were the first to model the emission from

a compact optically thick ($\tau_{UV} \sim 10^3$) dusty torus heated by a typical AGN continuum. The torus was considered as a cylindrical distribution of uniform density, extending from 4 to $\sim$ 40pc with optical depth corresponding to a hydrogen column density $N_H = 1.5 \times 10^{24} cm^{-2}$, in accordance with observational estimates. In the frame of their model the silicate emission feature was minimized for a narrow range of disk parameters and a limited range of viewing angles. Another shortcoming of the compact torus model was that it didn't produce broad enough infrared 'bump' compared to observations. Pier & Krolik (1993) had to add additional emitting components when modeling individual sources. However one of the main problems of their model was the enormous silicate absorption feature produced for edge-on views at the torus when increasing the equatorial optical depth. Such deep silicate features are not observed.

Calculations for homogeneous flared disks and extended tori ($100pc - 1kpc$) with moderate optical depths ($A_V \sim 6 - 60$) were done by Granato & Danese (1994) and Granato, Danese & Franceschini (1997) and the spectral properties of models were compared to observations by Fadda et al (1998). The model spectral shapes were in a reasonably good agreement with observed spectra, however the 10μm feature problem was not completely solved. Their studies showed that thick and compact cylinders are clearly ruled out as an AGN torus model. The main shortcoming of flared disk models, however, is the strong emission feature produced for pole-on viewing angles from the hot and optically thin disk surface layer. The emission feature could be suppressed in face-on views at the torus only at the expense of introducing silicate depletion in the inner parts of the torus (Granato & Danese 1994). Flared disks with sharp boundaries always produce a bi-modal distribution of model spectra: they are either Type 1 or Type 2, no matter how smooth the increase of the viewing angle.

Efstathiou & Rowan-Robinson (1995) developed and discussed in details the three different types of models: flared disks (with sharp boundaries), anisotropic spheres (with angular dust distribution), and tapered disks (a flared disk up to some radius after which the disk height remains constant). Flared disks with their

strictly bi-modal behavior and anisotropic spheres, failing to suppress the silicate emission feature and reproduce an acceptable spectrum, were rejected in favor of the tapered disk models. These types of models were able to minimize the silicate feature and reproduce the observed shapes of the AGN IR continuum of selected sources. However, for a better fit to observations the tapered disk models needed addition of extended conical dust component. These models also produced too steep near-infrared (NIR) slopes compared to observed spectra of Type 2 sources (Alonso-Herrero et al 2001, Alonso-Herrero et al 2003).

One of the major problems of homogeneous tori models is that they can't explain the recently observed enormous column densities measured in X-ray observations. Based on a large sample of Sy2 galaxies Bassani et al (1999) estimate a mean $\log N_H \sim 23.5$, with $23 - 30\%$ of the galaxies having column densities $N_H > 10^{24} cm^{-2}$. This means that the mean optical depth in the torus is $\tau_V \sim 400$ ($N_H \sim 10^{21}\tau_V\ cm^{-2}$) and there are cases where τ_V can exceed 1000. None of the homogeneous tori models can reproduce the observed spectra with such enormous optical depths without showing a very deep silicate absorption feature.

All radiative transfer models of the AGN dusty torus in the literature so far assume that it is homogeneous and solve the radiative transfer problem in the torus as a whole. The homogeneous tori models, however, couldn't satisfactory explain the observations. It is much more likely that the torus is clumpy, consisting of many dust clouds filling the torus volume. This is supported by theorethical considerations (Krolik & Begelman 1986 and Krolik & Begelman 1988) and observations (Tacconi et al 1994). Furthermore, a distribution of dusty clumps would provide a wider distribution in temperatures compared to a homogeneous torus, leading to a broader model spectrum, as required by observations. To demonstrate that a discrete dust distribution may suppress the silicate emission feature Rowan-Robinson (1995) calculated a composite spectrum of series of concentric shells and obtained a featureless quasar model spectrum. He considered the composite spectrum from a series of geometrically thin spherical dusty shells ($A_V \sim 5 - 10$) around the central source. Due to the narrow range of temperatures across each

of the shells the 10μm silicate feature is smeared in the resultant spectrum. However, there is a fundamental difference between clumps and series of concentric shells: a shell will emit isotropically and an observer will see only its dark side. In contrast, clump emission is anisotropic, since its illuminated and dark sides have very different temperatures.

Modeling of clumpy media is a numerically challenging task, performed with Monte Carlo techniques (see e.g., Witt & Gordon 2000 and references therein). However, it is based on probabilistic treatment of the photon interactions with the medium, and is computationally very intensive. We take a different approach to modeling a clumpy medium. We calculate the exact solutions of the radiative transfer in single dusty clumps and integrate over a given distribution of clumps in a toroidal volume.

1.3   Overview of the Thesis

Our model of a clumpy medium considers dusty clouds in a toroidal shape surrounding a central radiation source. The radiative transfer problem in each clump is solved exactly. We consider two populations of clouds: directly illuminated by the central source and indirectly heated by other clouds. The emission of directly heated clouds is obtained as angle-averaged emission of a dusty slab. The indirectly heated clouds are modeled as dusty spheres embedded in the average radiation field of the directly illuminated clouds. The emission of the medium is described by a source function, taken as a weighted sum of the two types of clouds. The overall emission is obtained by integration over the spatial distribution of clouds.

The material is organized as follows: our general approach toward modeling of clumpy media s in Ch.2; modeling the emission of AGN dusty tori is in Ch.3; comparison with observations is in Ch.4 and conclusions are in Ch.5. Slab radiative transfer calculation and our code DUSTY are discussed in the Appendices.

Chapter 2

Modeling Clumpy Media

The most fundamental quantity, that describes the radiation field at a point $\vec{r}$ of a medium, is intensity. This is the energy propagating in a solid angle in direction $\vec{l}$ per unit time per unit cross-section, per wavelength, $I_\lambda(\vec{r}, \vec{l})$, in units of $[W/(m^2 ster \mu m)]$. A dusty medium is described by a source function S_λ (defined as the ratio of emission and absorption coefficients), and an extinction coefficient, $k_\lambda = k_\lambda^{\mathrm{abs}} + k_\lambda^{\mathrm{sca}}$, including both absorption and scattering of radiation by dust particles. The change of intensity along a path segment ds depends on the properties of the medium and is found by solving the radiative transfer equation:

$$\frac{dI_\lambda}{ds} = k_\lambda(S_\lambda - I_\lambda) \tag{2.1}$$

The standard treatment of a dusty medium is under the assumption that dust is in thermodynamic equilibrium with radiation, and emits as a black-body with temperature T. Its emission is described by the black-body function $B_\lambda(T)$. If $\omega = k_\lambda^{\mathrm{sca}}/k_\lambda$ is the dust scattering albedo, the source function at some point in the medium is $S_\lambda(s) = (1 - \omega)B_\lambda(T(s)) + \omega J_\lambda(s)$, where $J_\lambda = \int I_\lambda d\Omega$ is the angle-averaged intensity at that point considering isotropic scattering. The extinction coefficient, which is the product of the number density of dust grains and their extinction cross-section, is related to the optical depth element of a segment ds, $d\tau_\lambda = k_\lambda ds$ and the mean free path (m.f.p.) in the dusty medium, $\ell = k_\lambda^{-1}$. Eq.(2.1) is solved for the intensity, given a boundary condition and dust properties.

2.1   Emission from a clumpy medium

Our general treatment of a clumpy medium is completely analogous to the standard radiative transfer formalism. We consider a medium of dusty clumps, all with the same optical depth, for simplicity. If n_c is the clump number density and A_c, the clump cross-sectional area, then the mean free path (m.f.p.) between clumps is $\ell = (n_c A_c)^{-1}$. The mean number of clumps, encountered in a segment ds along a given path s, is $d\mathcal{N}(s) = ds/\ell(s)$. Our only assumption is that the clumps are much smaller than the m.f.p. The m.f.p. dependence on the medium parameters determines the radiation propagation through the medium. Since the clump size never enters separately in our formalism, but only in a product with clump number density in the m.f.p., it is irrelevant as long the size is much smaller than the m.f.p. If S_λ is the source function in the segment, then the intensity generated
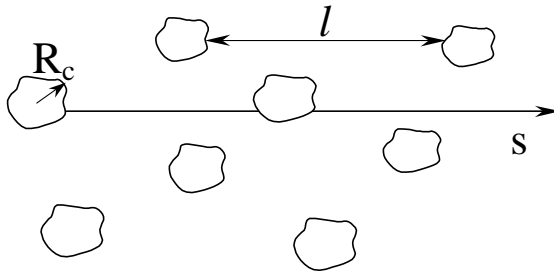
Figure 2.1: A clumpy medium consisting of clumps with a number density n_c and a cross-sectional area $A_c = \pi R_c{}^2$. The mean free path is determined by the product $n_c A_c$, $\ell = (n_c A_c)^{-1}$, therefore the clump size is irrelevant as long as the clump size is much smaller then the m.f.p.

along that segment is $S_\lambda d\mathcal{N}$. The emerging intensity depends on the probability P_{esc} that this radiation escapes without absorption by any other cloud. Following the treatment of a clumpy medium by Natta & Panagia (1984) we assume that the distribution of clumps along a line of sight (l.o.s.) obey the Poisson distribution. The probability to encounter exactly k clumps along a path containing $\mathcal{N}$ clumps

on average is

$$P_k = \frac{\mathcal{N}^k e^{-\mathcal{N}}}{k!} \qquad (2.2)$$

Thus the probability for escape after hitting k clumps is $\exp(-k\tau_\lambda)$. The overall escape probability is obtained by summing over all possible k's, $P_{\text{esc}} = \sum_{k=0}^{\infty} P_k e^{-k\tau_\lambda}$. The result is:

$$P_{\text{esc}} = e^{-t_\lambda}, \qquad t_\lambda = \mathcal{N}(1 - e^{-\tau_\lambda}) \qquad (2.3)$$

where $\mathcal{N} = \mathcal{N}(s) = \int_s d\mathcal{N}$ is the mean number of clumps along the rest of the path. In the limit of small τ_λ one gets $P_{\text{esc}} \approx e^{-\mathcal{N}\tau_\lambda}$. If τ_λ is high the probability saturates to $e^{-\mathcal{N}}$.

The emerging intensity from a segment ds is $P_{\text{esc}} S_\lambda d\mathcal{N}$. An observer at distance D, will intercept flux $F_\lambda = \int I_\lambda d\Omega$, where $d\Omega = dA/D^2$ is the solid angle subtended by the surface area element perpendicular to the line of sight.

Therefore the flux, observed at some distance D from the cloud distribution, is

$$F_\lambda = \frac{1}{D^2} \int dA \int e^{-t_\lambda} S_\lambda(s) d\mathcal{N}(s) \qquad (2.4)$$

This is the formal solution of the radiative transfer equation. Given the geometry, the flux can be calculated from this expression once the source function S_λ is known. Thus, our treatment of a clumpy medium is completely analogous to solving the radiative transfer problem in a continuous dusty medium. The only difference of our clumps with real dust grains is that there is no thermodynamic relation between the clump emission and absorption coefficients.

2.2 Single clump source function

We work in the approximation of clumps with size much smaller than the m.f.p. Furthermore, when a clump is observed at a large distance, its size is negligible. In this case the intensity is found as flux per unit solid angle, $I_\lambda = F_\lambda/d\Omega$. Therefore we calculate the clump source function from the ratio of its observed flux to the observed solid angle at a large distance.

The clumps in the dusty torus surrounding the AGN are heated by radiation from both the AGN and all other clumps. Therefore, at each position in the torus we consider two populations of clumps: i) directly illuminated by the AGN, with a source function $S_\lambda^{\rm d}$ and ii) diffusely heated by the average radiation field of the other clumps with a source function $S_\lambda^{\rm i}$.

For directly illuminated clumps with moderate to high optical depth the dust temperature is much higher on the illuminated face than any other part of the surface. Therefore the emission of such clumps is strongly anisotropic. It is described by the corresponding source function $S_\lambda^{\rm d}(r, \alpha)$ which depends on both distance r and the angle α between cloud position and the line of sight. The source function of a directly heated clump is obtained utilizing the exact solution of radiative transfer in a dusty slab. We calculate the solutions for a dusty slab illuminated by parallel rays (i.e. a very distant source) with typical AGN spectrum. The calculation is done with our code DUSTY (Ivezić, Nenkova & Elitzur 1999) for one-dimentional radiative transfer. A spherical clump directly illuminated by an external source has a reduced (two-dimentional) symmetry and can't be calculated with the current code. Since the clump shape is arbitrary, we model it by averaging the emission from illuminated slabs over all possible slab orientations.

Clumps whose line-of-sight to the AGN is blocked by another cloud will be heated only indirectly by diffuse radiation. We approximate the diffuse radiation field at distance r by averaging over α the emission $S_\lambda^{\rm d}(r, \alpha)$ of directly heated clumps at that distance. Secondary heating by the ambient radiation field of the other shadowed clumps is highly inefficient, because it involves long wavelengths, and thus can be neglected. The isotropic source function of an indirectly heated cloud, $S_\lambda^{\rm i}(r)$, is obtained from the exact solution for a sphere with constant density profile, embedded in the diffuse radiation field. Since this is a problem with spherical symmetry we calculate the emission of diffusely heated spherical clumps with our code DUSTY.

At distance r from the AGN the probability for unobscured view of the AGN is $p(r) = e^{-\mathcal{N}(r)}$, where $\mathcal{N}(r) = \int^r dr/\ell$ is the mean number of clumps to the AGN.

13

Therefore the source function for a given cloud optical depth can be represented as a weighted sum of the source functions of directly and indirectly heated clumps:

$$S_\lambda(r, \alpha) = p(r) \, S_\lambda^d(r, \alpha) + [1 - p(r)] \, S_\lambda^i(r) \qquad (2.5)$$

By constructing a 'synthetic' source function of a model clump, we account for the effects of direct and indirect heating.

The bolometric flux at a given distance from the source with luminosity L (the total energy emitted per unit time) is $F_e = L/(4\pi r^2)$. Clumps, directly heated by the external bolometric flux F_e reach their highest temperature, T_n, at the normally illuminated surface. There is a unique relation between this temperature and the heating flux F_e, (see eq.(6.2) in Appendix A), which is determined by dust properties, the clump optical depth and the spectral profile of the illuminating radiation. The inverse is also true: prescribing a surface temperature T_n uniquely defines an external bolometric flux F_e. This expresses the general scaling properties of the radiative transfer problem, thoroughly discussed by Ivezić & Elitzur (1997). Thus the scale of the overall clump emission is set by the heating AGN bolometric flux at a given point inside the medium, F_e

$$S_\lambda = F_e \, c_\lambda(L/r^2, \alpha, \tau_V) \qquad (2.6)$$

Scaling with the external bolometric flux has the advantage of producing distance independent spectral profiles, which we show in the following discussion. The two types of clumps and the way we obtain the source function are described next.

2.2.1   Directly illuminated clumps

The source function for directly illuminated clumps is obtained from the solutions of radiative transfer in a dusty slab. A dusty slab and a homogeneous dusty clump have the same basic property, that their emission is determined by a single parameter – the overall optical depth. The cloud has an arbitrary shape, therefore a realistic model of a single cloud at some position is obtained by averaging over slab orientations. The dust is taken as a typical Galactic dust (a 1:1 mixture graphite and silicates with MRN size distribution, Mathis, Rumpl & Nordsieck

14

(1977)). The optical depth of a single cloud is parametrized by the extinction
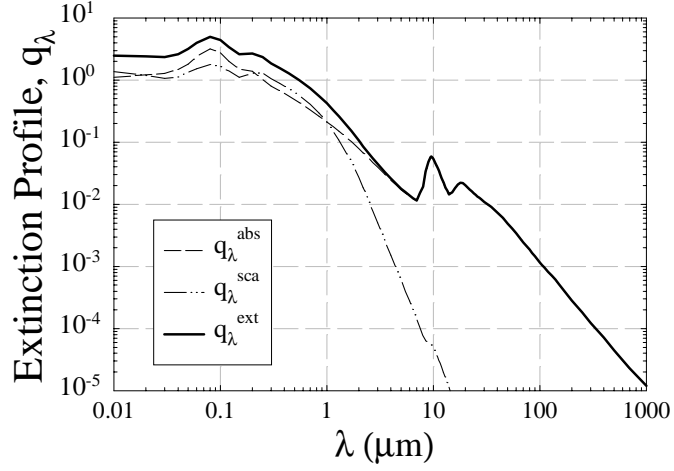
Figure 2.2: Extinction profile for Galactic type dust with its absorption and scattering components.

efficiency profile q_λ (Fig.2.2) and the visual optical depth τ_V, $\tau_\lambda = q_\lambda \tau_V$. Details of slab radiative transfer are discussed in Appendix A, here we only outline the procedure to obtain the source function of directly illuminated clumps. Consider a slab with area A_c with a normal on the illuminated side $\vec{n}$ and an observer in direction $\vec{o}$ at a distance $D \gg A_c$. The slab will emit flux toward the observer in direction with $\cos\theta_o = \vec{n} \cdot \vec{o}$, $F_\lambda = I_\lambda \cos\theta_o A_c/D^2$. For each prescribed angle of incidence θ_i we calculate the intensities for a set of θ_o and average over orientations:

$$S_\lambda^d = \int I_\lambda \cos\theta_o(\theta_i, \theta_o, T_n, \tau_V)\frac{d\theta_o}{\pi} \tag{2.7}$$

Sample source functions of directly illuminated clumps at low and high optical
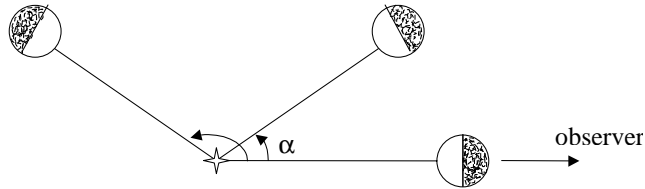
Figure 2.3: Clumps at a given distance from the AGN at an angle α in respect to the observer's direction. The clump emission is anisotropic since α determines the fractions of the clump's illuminated and dark sides and thus the observed spectral shape.
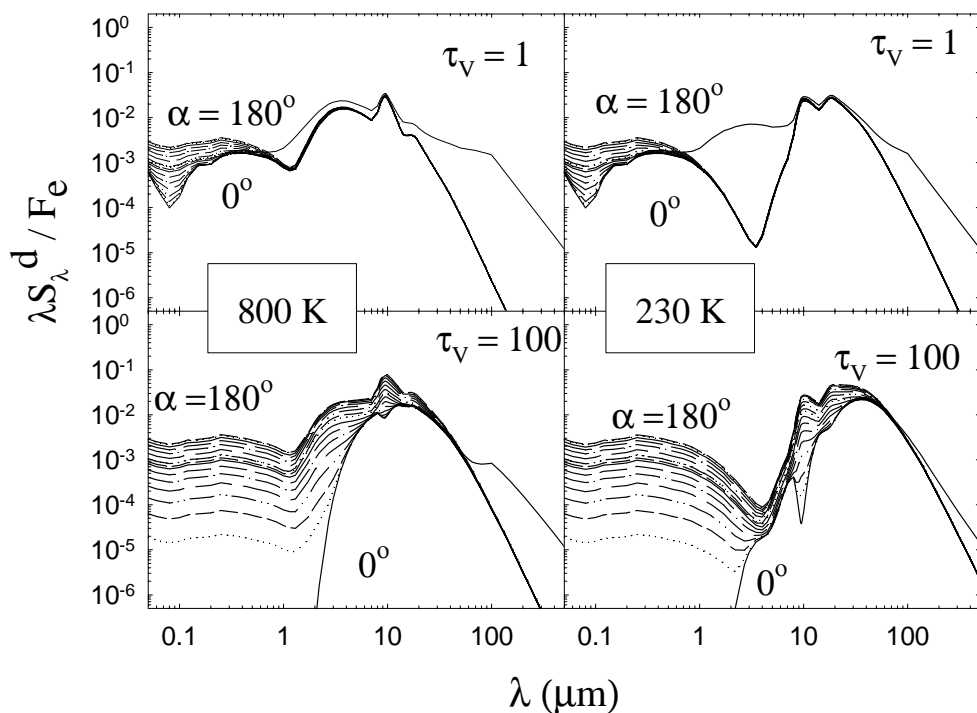
Figure 2.4: Emission of a single directly illuminated clump at two optical depths and two distances labeled by the maximal surface temperatures of the clumps. The angles α with respect to source and observer are given with a 12° step.

depth are shown in Fig.2.4 for a set of viewing angles. The source function is scaled by the external bolometric flux F_e at the slab surface thus producing distance independent spectral energy distributions (SED). For clump at a given position from the radiation source, its total optical depth τ_V is the only parameter of the SED.

The observed SED's are a direct result of the temperature distribution across the clump. The optical depth determines the temperature profile and the spectral properties of a single clump in the same way as for a single slab solution. The temperature profiles in a dusty slab saturate with increasing total optical depth (Fig.6.1). There is very little difference between the temperature profiles for τ_V= 100 and 500, and a further increase of the total slab optical depth produces profiles that are indistinguishable from the ones at τ_V= 500. As a result, increasing the optical depth of a single cloud above values of $\sim$ 100 or more will lead to a similar saturation of the spectral shapes of single clumps. The temperature on

the bright side of a normally illuminated slab is the same as the maximum surface temperature of a cloud at that position. Therefore it can be used to label distances as a result of its unique relation to the local bolometric flux F_e, eq.(6.2).

The procedure of slab emission averaging reproduces correctly the α-dependence of the observed fraction of illuminated area on the surface of a spherical-like object. The SEDs of directly illuminated clumps are clearly anisotropic, depending on the clump position (measured by α) in respect to the source and observer. At $\alpha = 0°$ only the dark side of the clump is seen, when increasing α the illuminated side provides larger contribution, proportional to the amount of observed bright area. Spectra from the bright clump side show much higher level of short-wavelength ($\lambda < 1\mu$m) emission compared to the spectra from the dark side. This is mostly scattered radiation from the hot surface layer of the cloud. The silicate emission feature from a single clump is the most pronounced when the whole illuminated side of the clump is seen by the observer ($\alpha = 180°$). Spectra from the dark, colder side show the dust radiation degraded toward longer wavelengths. The silicate feature is seen in absorption from the clumps dark side because colder dust layers are in front of the clump hotter regions.

The silicate feature is discussed in more detail in Ch.4, here we will only note the limited depth of the feature when clumps are viewed from their dark side. This is precisely one of the major differences of the clumpy distribution of clumps with a homogeneous torus. In model spectra of homogeneous tori the depth of the feature can become enormous at large optical depths due to the large temperature gradient across the torus. On the contrary, for a distribution of clumps the feature can not become infinitely deep since it is saturated in a single clump (Fig.6.4). The saturation results from the flat temperature profiles established across the clump. Consequently, the absorption feature will be saturated in the emission from a distribution of clumps. Thus the optical depth in the torus can become huge and nevertheless the absorption feature will not be deep. This is one of the main advantages of a clumpy medium towards explaining observational results.

2.2.2   Diffusely heated clumps

The other type of clumps is heated indirectly by the ambient diffuse radiation of the directly illuminated clumps. We approximate the diffuse radiation field at a distance r from the source by averaging over α the emission $S_\lambda^{\mathrm{d}}(r, \alpha)$ of directly heated clumps. The isotropic source function of an indirectly heated cloud, $S_\lambda^{\mathrm{i}}(r)$, is obtained from the exact solution of radiative transfer in a sphere with constant density profile, embedded in the diffuse radiation field. If $F(R)$ is the flux the sphere emits from its surface, then $S_\lambda^{\mathrm{i}} = F(R)/\pi$ is the intensity of isotropic emission whose half-flux is $F(R)$. $F(R)$ does not depend on R, only on the overall τ_{V}. Fig.2.5 shows the emission of diffusely illuminated clumps at two optical depths and a set of distances. The distances are labeled by the temperatures of a normally illuminated slab at that position. The indirectly heated clumps emit isotropically and the spectral shapes for a given optical depth depend on the distance to the source, $S_\lambda^{\mathrm{i}} = S_\lambda^{\mathrm{i}}(r)$. The heating is controlled by
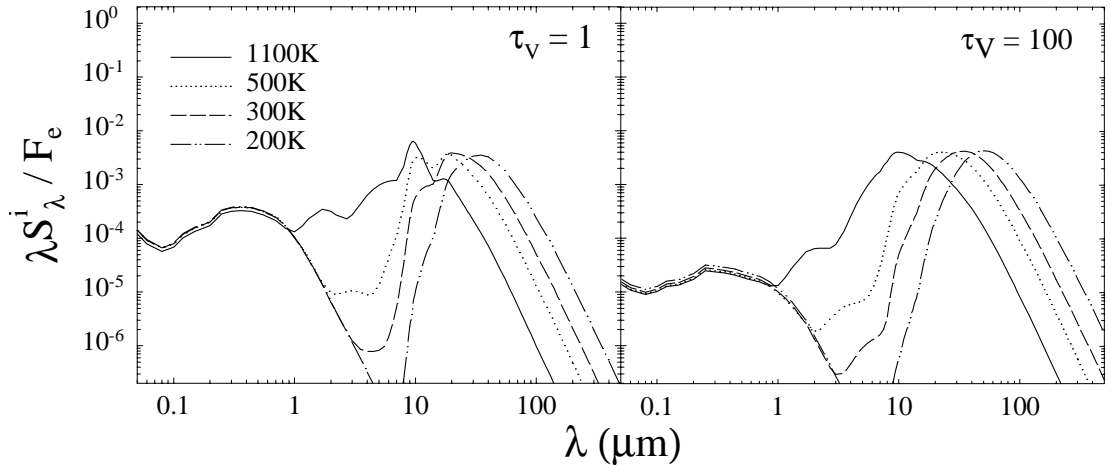
Figure 2.5: Emission of diffusely illuminated clumps for a set of distances and two optical depths. The distances are labeled by the temperatures of a normally illuminated slab at that position.

the short wavelengths as a result of the dust absorption profile. The emission of indirectly heated clumps is shifted toward longer wavelengths since it is re-processed radiation. Therefore, secondary heating of indirectly illuminated clumps

18
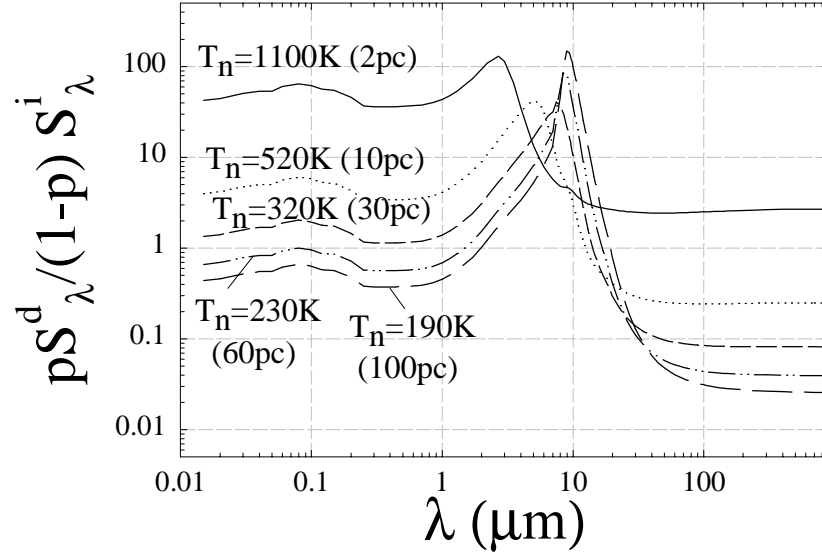
Figure 2.6: Ratio of the two components of the 'synthetic clump' source function, where S_λ^d is taken at $\alpha = 90°$.

from the ambient field of other shadowed clumps can be neglected. In other words, there is no need of higher order terms in the source function. As seen from Fig.2.6, the main contribution to the 'synthetic clump' source function comes from the directly illuminated clumps for all significant wavelengths.

Chapter 3

Modeling the Torus Emission

3.1   Model parameters
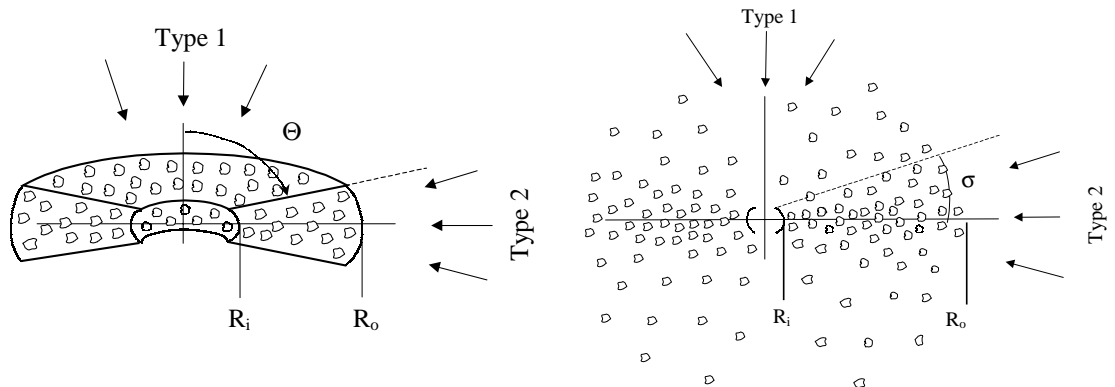
Figure 3.1: Clumps with an optical depth τ_V occupy a toroidal volume enclosed between an inner and outer radii, R_i and R_o, respectively. The torus can have sharp or smeared conical boundaries. The first case is described by the cone half-opening angle, while an angular distribution of clumps has a width σ. These, along with the total number of clouds $\mathcal{N}_T$ along an equatorial ray, are parameters of the distribution.

We consider a toroidal distribution of clumps around an AGN (Fig.3.1) between an inner and outer radius, R_i and R_o, respectively. The clouds have an angular distribution $\Phi(\beta)$, with β measured from the equatorial plane of the torus, and a width σ. The radial distribution is taken as a power law. Each cloud has an optical depth τ_V. The total number of clouds along an equatorial ray is $\mathcal{N}_T$.

The overall emission of the clouds distribution is found by integration over the distribution, with the already found source function at each point of the clumpy medium, eq.(2.5). As explained in Ch.2, the external bolometric flux F_e at a point in the medium is the natural scale of the source function with a spectral shape c_λ. The inner radius of the torus, R_i defined as the dust sublimation boundary, is the scale for all quantities with dimension of lengths. It depends on AGN luminosity as

$$R_i = 1.02\sqrt{L_{12}} \left(\frac{1400K}{T_i}\right)^2 pc \tag{3.1}$$

Scaling the surface element $dA = da/R_i{}^2$, the radius $y = r/R_i$ and the line-of-sight (l.o.s.) coordinate $u = s/R_i$, the flux observed in direction i and at distance D, eq.(2.4), is:

$$F_\lambda^T(\tau_V, i) = F_{AGN} \int \frac{da}{y^2} \int e^{-t_\lambda(u)} c_\lambda(u) \frac{R_i du}{\ell} \tag{3.2}$$

Here $F_{AGN} = L/(4\pi D^2)$ is the intrinsic AGN bolometric flux at the observer position.

The radial and angular cloud distributions are independent and can be represented by a product of the functions of y and angle β from the equatorial plane. Thus, the m.f.p. can be expressed as

$$\frac{1}{\ell} = \frac{\mathcal{N}_T}{R_i} \Phi(\beta)\Lambda(y), \qquad \text{with} \quad \Phi(0) = 1, \quad \int_1^Y \Lambda(y)dy = 1 \tag{3.3}$$

where $Y = R_o/R_i$ is the radial extent of the torus. For a radial dependence function we employ a power law, $\Lambda(y) = Cy^{-q}$, with the constant C found from the normalization condition to be $C = (1-q)/(Y^{1-q}-1)$ for $q \neq 1$, and $C = 1/(lnY)$ for $q = 1$.

With the m.f.p. from 3.3 the final expression for the torus emission function is:

$$f_\lambda^T(\tau_V, i) = \frac{F_\lambda^T(\tau_V, i)}{F_{AGN}} = \mathcal{N}_T \int da \int e^{-t_\lambda(u)} c_\lambda(u) \Phi(\beta)\Lambda(y) \frac{du}{y^2} \tag{3.4}$$

where $\beta = \beta(u)$ and $y = y(u)$. Here the escape probability exponent,

$$t_\lambda(u) = (1 - e^{-\tau_\lambda})\mathcal{N}(u) \tag{3.5}$$

depends on the mean number of clouds $\mathcal{N}(u)$ from a point along the path to the surface and on the optical depth of each cloud $\tau_\lambda = q_\lambda \tau_V$:

$$\mathcal{N}(u) = \mathcal{N}_T \int_u^{u_o} \Phi[\beta(u')]\Lambda[y(u')]du' \qquad (3.6)$$

We consider an angular distribution of the clumps since this is a more likely structure compared to a torus with sharp boundaries. A way to smear the torus boundaries is to consider angular dependence of the type shown in Fig.3.2:

$$\Phi(\beta) = \exp - \left|\frac{\beta}{\sigma}\right|^p \qquad (3.7)$$

where β is the angle from the equatorial plane of the torus and σ is the width of the distribution. $p = 2$ is a slightly modified Gaussian (our width $\sigma = \sqrt{2}\sigma_G$ of the usual Gaussian). Increasing p brings the distribution closer to the case of a torus with a sharp boundary and with cone half-opening angle $\Theta = 90° - \sigma$.

Parameters of the cloud distribution are the total number of clouds along an equatorial radius, $\mathcal{N}_T$, the power q of the radial power law, the angular distribution width σ and the extent of the torus $Y = R_o/R_i$.

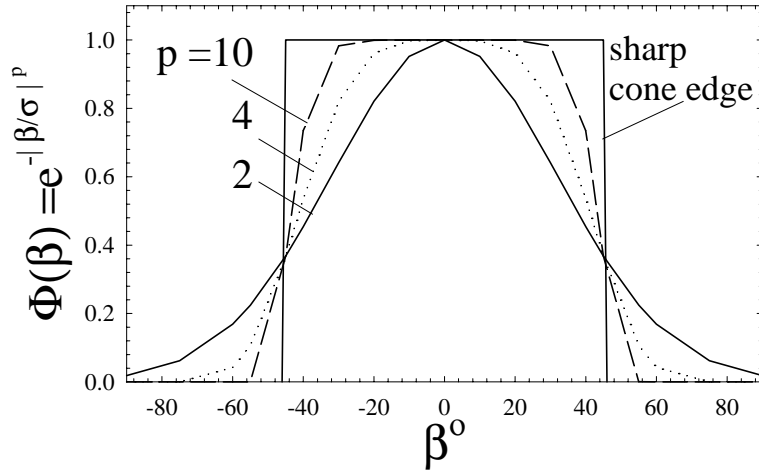Figure 3.2: Angular dependence of the density distribution. β is the angle from the equatorial plane of the torus with a cone opening angle $90° - \sigma$.

Since the medium is clumpy, there is always a non-zero probability of seeing the AGN along a ray at any viewing angle. However, for rays crossing less dense torus parts, this probability will be much higher, as determined by the angular

density distribution function of clouds $\Phi(\beta)$. For a torus with sharp cone boundaries the AGN will be completely visible for all rays crossing the opening cone. Therefore, we add the normalized AGN spectral shape f_λ^{AGN} (λf_λ = constant in the wavelength range $0.01 - 0.1$ μm and $\lambda f_\lambda \propto \lambda^{-0.5}$ for 0.1-100 μm), to the calculated torus spectra for viewing angles with a higher probability of 'seeing' the AGN. For a modified Gaussian (with any power p) this is the case of viewing angles $i < 90° - \sigma$, when $\Phi(90° - i) < e^{-1} = 0.37$. For a torus with sharp boundaries, the normalized AGN spectral shape is added when $i < \Theta$.

Below is a summary of our model parameters, outlined for convenience.

- i - viewing angle measured from the azimuthal axis. Our results show that the viewing angle is the parameter that determines the type of observed spectrum.

- Clump parameters:

  1. τ_V - single clump optical depth at the visual $(0.55\mu$m) wavelength. Models were produced for τ_V in the range $10 - 500$.

  2. $\mathcal{N}_T$ - total number of clumps along an equatorial ray. The range of values considered in the modeling was $2 - 15$. Values as high as 20 or more would produce SEDs with an IR 'bump' shifted too much in the far-IR and lack of near-IR emission, which do not seem to match observations.

- Parameters of the distribution of clumps:

  1. $Y = R_o/R_i$ - the torus relative size, where R_o is the outer radius of the torus. Models were produced for $Y = 10 - 250$. $Y = 4$ was also checked, however it doesn't seem plausible, since the IR emission is not broad enough to comply with observations. R_i is the torus inner radius, determined by dust sublimation. For dust sublimation temperature of $1,400K$ and AGN luminosity of $10^{12}L_\odot$ R_i is 1 pc, eq.(3.1). It is kept

fixed at this value in all model results. The inner radius of the torus is the scale for all quantities with dimension of lengths.

2. q - the power of the radial distribution function, $\Lambda(y) = Cy^{-q}$. We considered values of $q = 0 - 2$.

3. p - the power of the angular distribution function $\Phi(\beta)$, eq.(3.7), where β is measured from the equatorial plane. $p = 2$ is a Gaussian, higher values of p bring the distribution closer to a torus with sharp boundaries. Two main sets of results were produced: for a Gaussian ($p = 2$) and for a torus with sharp boundaries.

4. σ - the angular distribution width, taken in the range of $15° - 75°$. For a torus with sharp boundaries $\Theta = 90° - \sigma$ is the cone half-opening angle.

3.2   Model spectra

3.2.1   Dependence on viewing angle

In accordance with the Unified Model we find that, given the cloud distribution and torus parameters, the major parameter that determines the type of the SED is the viewing angle (measured from the torus azimuthal axis).

The two general types of spectra are for viewing angles that 'see' the AGN ($i < 90° - \sigma$) and those that cross the torus ($i > 90° - \sigma$). The first reproduce a typical Type 1 spectrum, while the second show a Type 2 spectrum. As expected, a sharp boundary torus has little dependence on viewing angle except when the l.o.s. crosses the torus (Fig. 3.3, left panel). This produces a bi-modal distribution of spectral shapes, similar to the bi-modal spectra of homogeneous flared disks (see, e.g., Granato & Danese (1994)). In other words, if the rays cross the torus they will always hit a cloud. Since the single cloud optical depths are large, the spectra will not be very different, and this is what we obtained from the model. The greater variety in the observed spectral shapes of Type 2 sources is better
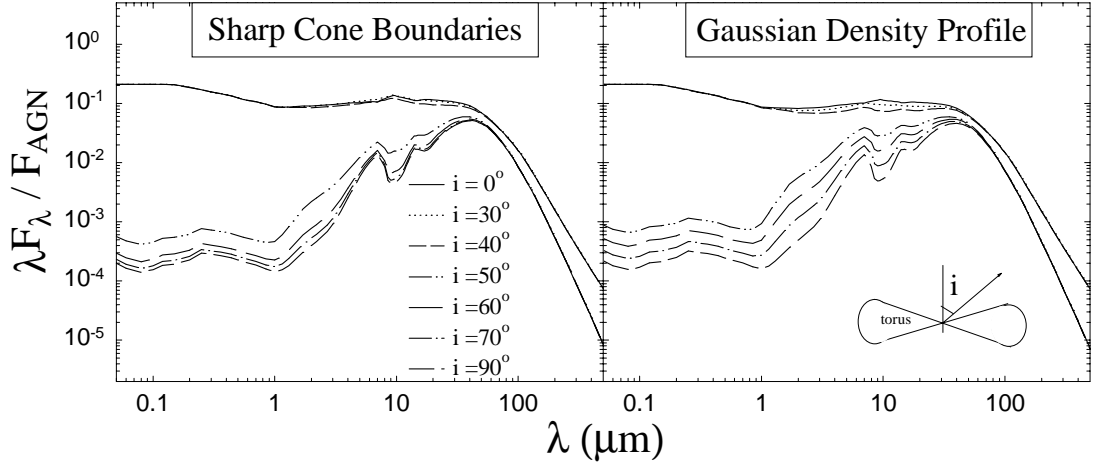
Figure 3.3: Results for a torus with sharp boundaries and 45° half-opening angle and a Gaussian angular distribution of the clouds with $\sigma = 45°$. Single cloud optical depth $\tau_V = 60$; total maximum number of clouds $\mathcal{N}_T = 5$; extent of the torus $Y = 100$.

reproduced by a Gaussian angular distribution. The angular density distribution of clouds modifies the probability of hitting a cloud, therefore a larger scatter of spectral shapes is obtained, even for a high single cloud optical depth.

Note the vanished 10μm silicate emission feature in the spectra of Gaussian distribution for viewing angles $i < 90° - \sigma$. A weak emission feature can be seen, however, in the case of clouds in a torus with sharp boundaries. Clouds seen mostly at their illuminated sides are the source of the emission feature therefore the escape probability will determine the extent of the feature suppression. A Gaussian distribution introduces a non-vanishing probability of attenuation by a cloud on the way of rays in the cone. Therefore the emission feature will be suppressed even more, compared to the case of clouds in a cone with sharp edges.

For viewing angles intercepting denser torus parts, $i > 90° - \sigma$, the sharp boundary torus is thicker than a Gaussian, and the increased obscuration along a ray leads to steeper profiles with a negligible spread in angles. Rays passing through denser torus parts when increasing the viewing angle produce a deepening silicate absorption feature. Note, however, that the depth is limited, due to the saturation of the depth in a single clump.

25

The ratio of model SED's for the two limiting viewing angles gives an upper limit estimate for the anisotropy of the emission of Type 1 and Type 2 sources. The anisotropy decreases with increasing the wavelength as expected, since the torus becomes optically thin at wavelengths beyond $\sim 30\mu$m for τ_V up to about 500. This agrees also with the homogeneous tori models. The observationally inferred anisotropy, based on luminosities at a given wavelength for Sy1 and Sy2 sources should be less, since there is a variety in the possible viewing angles.

3.2.2 Dependence on cloud parameters

Here we consider the effect on the SED of the total number of clouds, $\mathcal{N}_T$, along an equatorial ray and of the single cloud optical depth, τ_V, even though $\mathcal{N}_T$ is, in fact, a global cloud distribution parameter. Representative model spectral energy distributions (SED) are shown in Fig.3.4 for sets of viewing angles and total number of clouds $\mathcal{N}_T$ along an equatorial ray. SEDs, corresponding to the ones of Type 1 and Type 2 AGN, are produced as a result of viewing angle $i < 90° - \sigma$ (i.e. 'seeing the AGN') or l.o.s. crossing the denser parts ($i > 90° - \sigma$). The IR bump, so typical in observations of both types of sources, is well defined. The short-wavelength parts in Type 2 SED are due to diffuse scattering from the illuminated sides of the clouds. This is unlike the homogeneous tori models, which do not show any emission at $\lambda < \sim 1\mu$m due to their high optical depths in a continuous medium. Our model tends to maximize the scattering because the cloud emission is based on emission of a slab at various orientations toward source and observer. The slab, when viewed from its illuminated side, shows a high level of reflected short-wavelength light (see Fig.6.3 in Appendix A, showing the slab emission). This, in fact, is not a shortcoming of our model. Instead it represents the correct physical picture of trapping the scattered short-wavelength radiation as a result of multiple scattering among clouds.

Our model is a single-phase model, i.e. it considers the torus volume filled with clouds only. We do not consider additional inter-cloud medium because of the high degree of uncertainty in its nature and properties. There is no conclusive
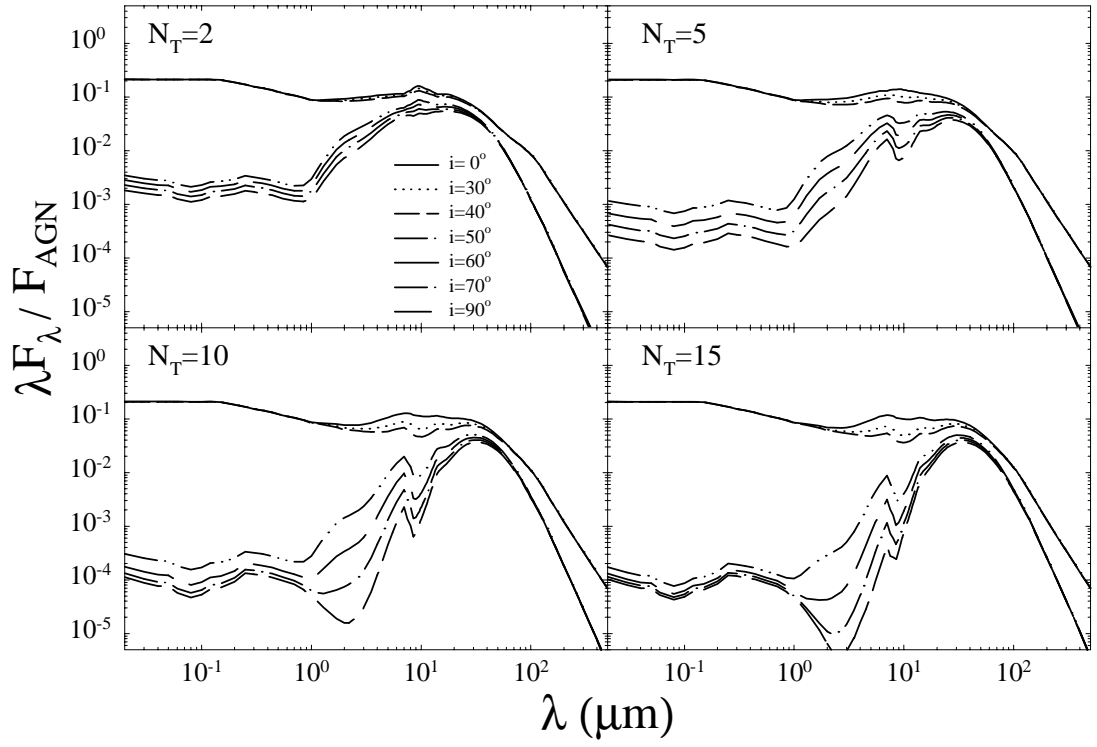
Figure 3.4: Model spectra for torus extent of $Y = 100$. Gaussian angular distribution of the clouds with $\sigma = 45°$, radial power $q = 1$, single cloud optical depth $\tau_V = 60$.

evidence for the necessity of introducing such an additional factor. However, if we assume that this medium has a Galactic extinction curve and an optical depth of $\tau_V \sim$ a few, the additional attenuation is sufficient to remove the UV and visual parts of the model SED.

Comparing Fig.3.4 and Fig.3.5 the effect of the total number of clouds on the SED is stronger than the effect of a single cloud optical depth. The near- and mid-IR slopes are determined predominantly by $\mathcal{N}_T$. The single cloud optical depth for a fixed $\mathcal{N}_T$ (Fig.3.5) creates 'a fan' of additional spectral shapes. There seems to be a degeneracy of the shapes in respect to the two main parameters and only a systematic statistical search among the model families is able to distinguish between the effects of $\mathcal{N}_T$ and τ_V.
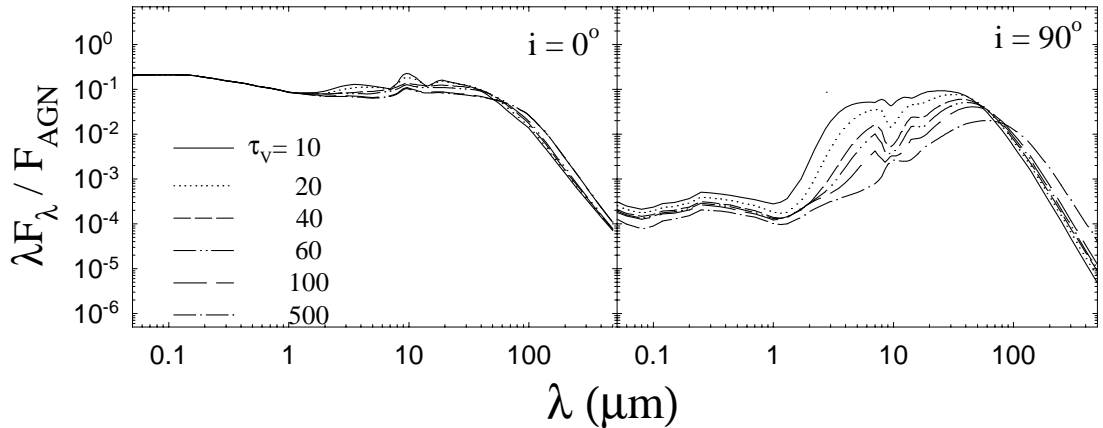
Figure 3.5: Dependence on single cloud optical depth. Gaussian density distribution with $\sigma = 45°$ radial power $q = 1$, $Y = 100$, $\mathcal{N}_T = 5$.

Increasing $\mathcal{N}_T$ increases the probability of obscuration along the l.o.s. and has the greatest effect on the near-IR slopes. This is a direct result of the escape probability spectral profile and its dependence on cloud parameters (eq.(2.3)). The effect of P_{esc} can be illustrated by showing the dependence along an equatorial ray in Fig.3.6. The spectral and radial profiles of P_{esc} are determined by the interplay between the single cloud optical depth and the total number of clouds along a given path. In other words, P_{esc} includes both the single cloud parameter τ_V and the overall distribution parameter $\mathcal{N}_T$. Once the optical depth τ_λ of a single cloud

exceeds ~ 2 at a given wavelength, the dominant parameter at that wavelength becomes the number of clouds $\mathcal{N}_{\mathrm{T}}$. For the considered dust optical depth profile τ_{V} of 100 means $\tau_{5\mu m} \sim 2$ and $\tau_{30\mu m} < 1$ (Fig.2.2). P_{esc} saturates up to the mid-IR for cloud optical depths exceeding ~ 200.
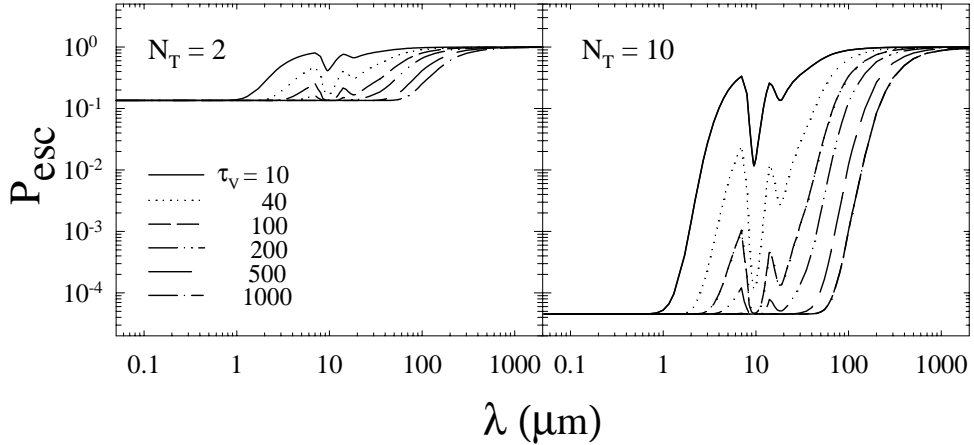
Figure 3.6: The escape probability along an equatorial ray. Its spectral profile shapes the emission of the ensemble of clouds.

3.2.3 Dependence on distribution

Parameters related to the distribution geometry are the extent of the torus $Y = R_{\mathrm{o}}/R_{\mathrm{i}}$, the radial density profile and the width of the angular distribution, σ. The effect of the radial extent, $Y = R_{\mathrm{o}}/R_{\mathrm{i}}$, is on the width of the torus emission (Fig.3.7), since increasing Y means redistribution of the same number of clumps further away from the AGN. As a result, the decreased clump temperature leads to shift of the emission further in the IR. For Type 1 viewing angles the effect is not too pronounced, although an increase of the IR emission width can be seen. For Type 2 viewing angles the position of the maximum emission shifts toward longer wavelengths and the silicate absorption feature is slightly modified as result of that. Comparison with data for Type 1 sources suggest that the size can not be less than 10 pc for the AGN luminosity of $L_{12} = 1$ that we consider. Sizes smaller than this would not produce enough mid- and far-IR emission.

Radial power laws, $\Lambda(y) \sim y^{-q}$, in the range $q = 0 - 2$ were considered. Flat density means more cool clouds will be farther away from the AGN. This will
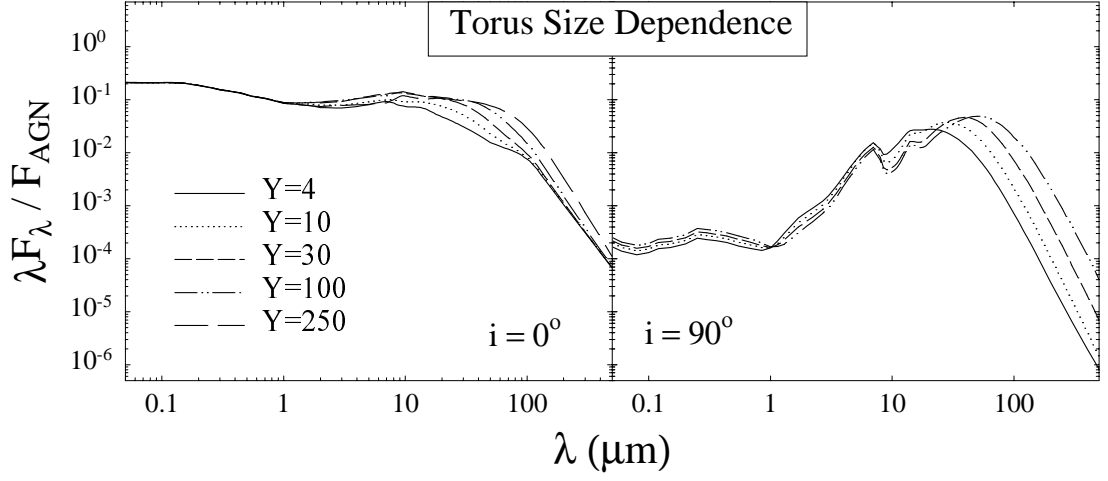
Figure 3.7: SED dependence on $Y = R_o/R_i$. Gaussian angular distribution of the clouds with $\sigma = 45°$, radial power $q = 1$, single cloud optical depth $\tau_V = 60$, $\mathcal{N}_T = 5$.
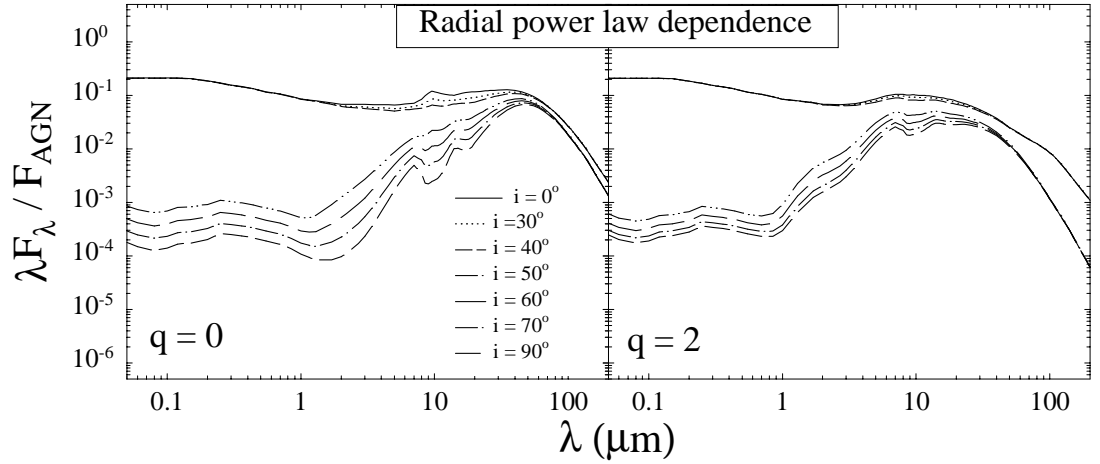
Figure 3.8: SED dependence on the radial density distribution. Model spectra for torus extent of $Y = 100$, Gaussian angular distribution of the clouds with $\sigma = 45°$, single cloud optical depth $\tau_V = 60$, $\mathcal{N}_T = 5$.

increase the amount of far-IR emission while reducing the near-IR emission, since the total number of clouds is kept the same (Fig.3.8, left panel). Steeper density distribution of clouds will decrease the amount of clouds in the outer torus regions, while increasing them in the inner, hotter parts. Therefore the near-IR emission will increase, and the far-IR bump will be reduced (Fig.3.8, right panel).

The half-width of the angular distribution is σ. Its effect is shown in Fig.3.9 for three types of tori: very thin ($\sigma = 15°$), intermediate ($\sigma = 30, 45°$) and a thick, "puffy" torus ($\sigma = 75°$). The AGN spectrum will be seen with much higher
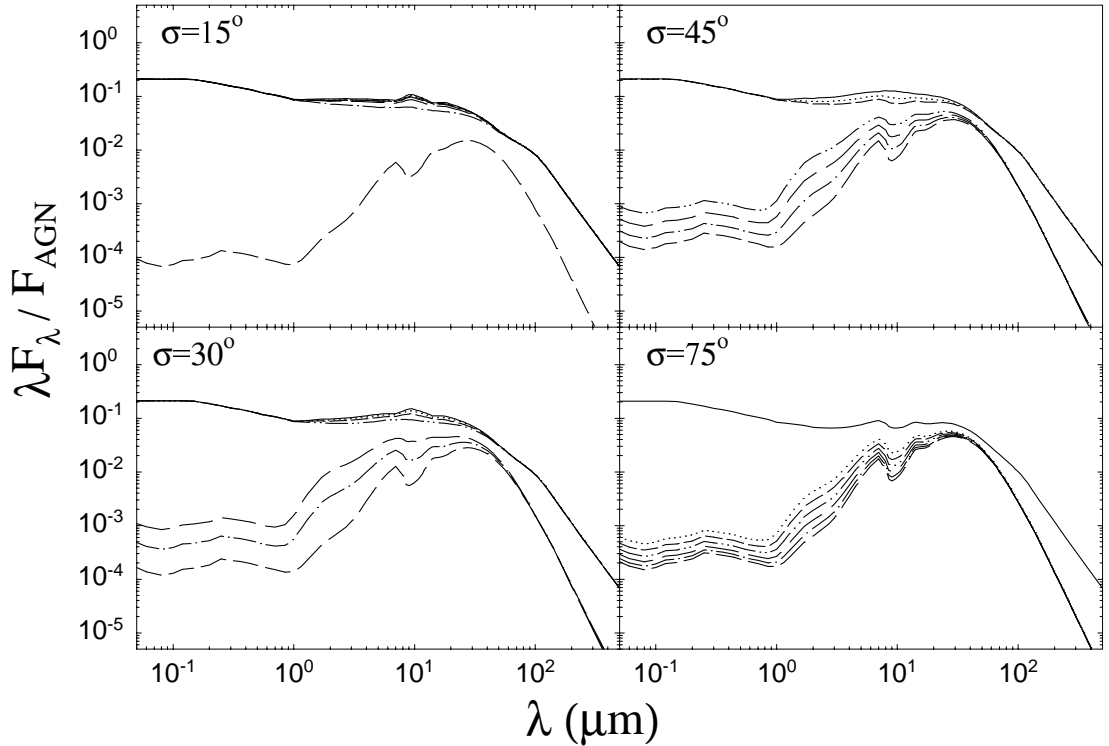
Figure 3.9: Dependence on the width σ of the angular distribution of clouds. Lines correspond to the same set of viewing angles in $i = 0° - 90°$ as in the previous Fig.3.8. Models for a radial power law $q = 1$, $Y = 30$, $\tau_V = 60$, $\mathcal{N}_T = 5$.

probability for viewing angles $i < 90° - \sigma$, therefore for $\sigma = 15°$ only edge-on views will produce a Type 2 spectrum. Generally "thin" ($\sigma = 15°$) tori tend to show the silicate feature in emission, while it is turning into absorption even for a face-on view in thicker tori and large $\mathcal{N}_T$.

In summary, our model SEDs reproduce the broad IR bump extending to $\sim$

100 μm, as observed. Furthermore, the 10 μm feature appears in absorption for viewing angles intercepting denser torus parts ($i > 90° - \sigma$). It is smeared out in axial viewing in spite of its prominence in emission from directly-heated individual clouds. The reason is that emission feature is produced from the illuminated side of the clouds, and the more of this side is seen, the more prominent the emission feature. These are clouds around an equatorial axis of the torus (viewed pole-on) and further away from the observer. However, the emission of these clouds has a higher probability of obscuration by the foreground clouds in the torus, which do not show an emission feature due to their respective orientation to the observer.

Our modeling results support the statement of the Unified Model that the main factor discriminating between Type 1 and 2 SED is the viewing angle. The probability of seeing the AGN is much higher when the l.o.s. crosses the torus cone, thus giving rise to a Type 1 spectrum. Increasing the viewing angle drastically reduces this probability and produces a Type 2 spectrum and a silicate absorption feature.

It is important to note that the clump size R_c doesn't enter in our considerations. Furthermore, the total mass of all clumps in the system can be found without referring to the size of a single clump. An estimate of the total mass can be found from $\int m_c n_c d^3 r$ with $m_c = n_H m_H V_c$. Using the standard gas-to-dust ratio $n_H = 10^{21} \tau_V / R_c$, the total mass is:

$$M_{tot} = 2\pi 10^{21} m_H \tau_V \mathcal{N}_T R_i^2 \int \Phi(\theta) d\cos\theta \int \Lambda(y) y^2 dy \tag{3.8}$$

Estimating the integral over distribution,

$$M_{tot} = 2.5 M_\odot \tau_V \mathcal{N}_T L_{12} \sin\sigma Y^{3-q} \tag{3.9}$$

For a torus with sharp boundaries and $\sigma = 45°$, with typical model values of $q = 1$, $\tau_V = 100, \mathcal{N}_T = 5$, the total mass is of the order of $M_{tot} = (2.4 \times 10^5 - 1.3 \times 10^7) M_\odot$ for $Y = 10 - 100$.

Our model is developed under the assumption that the cloud size is much less than the m.f.p., $R_c \ll \ell$. The distribution is described by q and $\mathcal{N}_T$, and individual clouds – by their optical depth τ_V. To relate to the real AGN tori, an estimate of

possible cloud sizes can be done as follows. If V_c is the volume of a single cloud, and $n_{\rm c}$ is the cloud number density, the volume filling factor (the volume fraction occupied by clouds) is

$$\phi = n_{\rm c}V_c = n_{\rm c}A_{\rm c}R_{\rm c} = R_{\rm c}/\ell \tag{3.10}$$

Thus our calculations apply to small filling factors, $\phi \ll 1$. The m.f.p. at the inner torus radius is $\ell(R_{\rm i})/R_{\rm i} = (1/\mathcal{N}_{\rm T}) \int_1^Y y^{-q}dy$. Thus a model with $q = 1$, $\mathcal{N}_{\rm T}= 5$ and $Y = 100$ has $\ell(R_{\rm i}) = 0.9R_{\rm i}$ pc. A realization of this model, for example, can be a constant filling factor of $\phi = 0.1$ throughout the torus so that $R_{\rm c} = 0.09yR_{\rm i}$. The clouds then can vary from $R_{\rm c} \sim 0.1$ pc in the torus inner regions to $R_{\rm c} \sim 10$ pc at the outer edge. The cloud gas density will decrease correspondingly from 3×10^5 to 3×10^3 cm^{-3}, in order to have the same cloud $\tau_{\rm V}$.

The total number of clouds in the system can be found from $\int n_{\rm c}d^3r$:

$$N_{tot} = 2\mathcal{N}_{\rm T}R_{\rm i}{}^2 \int \frac{\Phi(\theta)\Lambda(y)}{R_{\rm c}{}^2}y^2dy\,d\cos\theta \tag{3.11}$$

In our model the cloud size is a small fraction of the m.f.p., but can not be independently determined. Substitution of $R_{\rm c} = \phi\ell$ and m.f.p. from eq.(3.3) gives explicit dependence on the filling factor:

$$N_{tot} = 2\mathcal{N}_{\rm T}{}^3 \int \frac{\Phi^3(\theta)\Lambda^3(y)}{\phi^2}y^2dy\,d\cos\theta \tag{3.12}$$

Thus the specific clump parameters number density $n_{\rm c}$ and size, $R_{\rm c}$, are replaced by the equivalent ones: the m.f.p. ℓ and filling factor ϕ. Note, that the filling factor does not appear in the expression for total mass in clumps, eq.(3.8).

3.3 Brightness profiles and maps

Along with the SED's, surface brightness distributions, b_λ, are an output of the model as well, since the integral over distribution, eq.(3.4) is:

$$f_\lambda^T = \int b_\lambda da \tag{3.13}$$

Expressing the area element $da = d\Omega/\theta_i^2$, where $\theta_i = R_i/D$ is the angular size of the inner radius of the torus, the relation of our model function b_λ to the observed intensity becomes

$$I_\lambda = \frac{F_{AGN}}{\theta_i^2}b_\lambda = F_{e,i}b_\lambda \qquad (3.14)$$

where $F_{e,i}$ is the bolometric flux at the inner torus boundary. It is directly related to the temperature at the inner boundary from the scaling relation, eq.(6.2):

$$F_{e,i} = \frac{4\sigma T_i^4 q_P(T_i)}{q_{ae}}\frac{1}{\psi(\tau_V)} \qquad (3.15)$$

T_i is the maximum temperature of a directly illuminated cloud at R_i, and $\psi(\tau_V)$ is the scaling function which saturates with increase of optical depth. $q_P(T_i)/q_{ae}$ is the ratio of the spectral averaged absorption efficiencies: $q_P(T_i)$ is averaged with the emission of dust at temperature T_i and q_{ae} is with the illuminating AGN spectral shape. Substituting our model values in the expression for I_λ one can obtain the relation of the observed intensity to T_i. For practical purposes the model intensities can be converted to $[\text{Jy/mas}^2]$ (Jansky per square milliarcsecond) using $1\text{ Jy} = 10^{-26}\text{W}/(\text{m}^2\text{ Hz})$ and $1\text{ rad} = 2.06\times10^8$ mas:

$$I_\nu\left[\frac{Jy}{mas^2}\right] = 0.3\lambda[\mu m]b_\lambda\left[\frac{T_i}{1400K}\right]^4\frac{q_{a,\lambda}(T_i)}{q_{a,\lambda}(1400K)}\frac{1}{\psi(\tau_V)} \qquad (3.16)$$

Below are results for intensity profiles and contours. The wavelength dependence of intensity contours for a face-on viewed torus is shown in Fig.3.10. The observed size of the torus is the smallest at near-IR, because the amount of scattered radiation decreases significantly (Fig.2.2) while dust emission, even though increasing, is still not too much. These wavelengths ($\sim 2 - 3\mu m$) are the region where dust emission takes over scattering.

Observations have about 2-3 orders of magnitude dynamical range. As seen from the contour maps and profiles the two different torus sizes look very similar in their inner parts, where the intensity decreases about that much. This implies that it would be difficult to achieve a conclusive estimate for the outer radius based on observations, especially in the near-IR, where most of the current imaging is performed. Observations in far-IR (e.g. at $60\mu m$) may reveal size closer to the
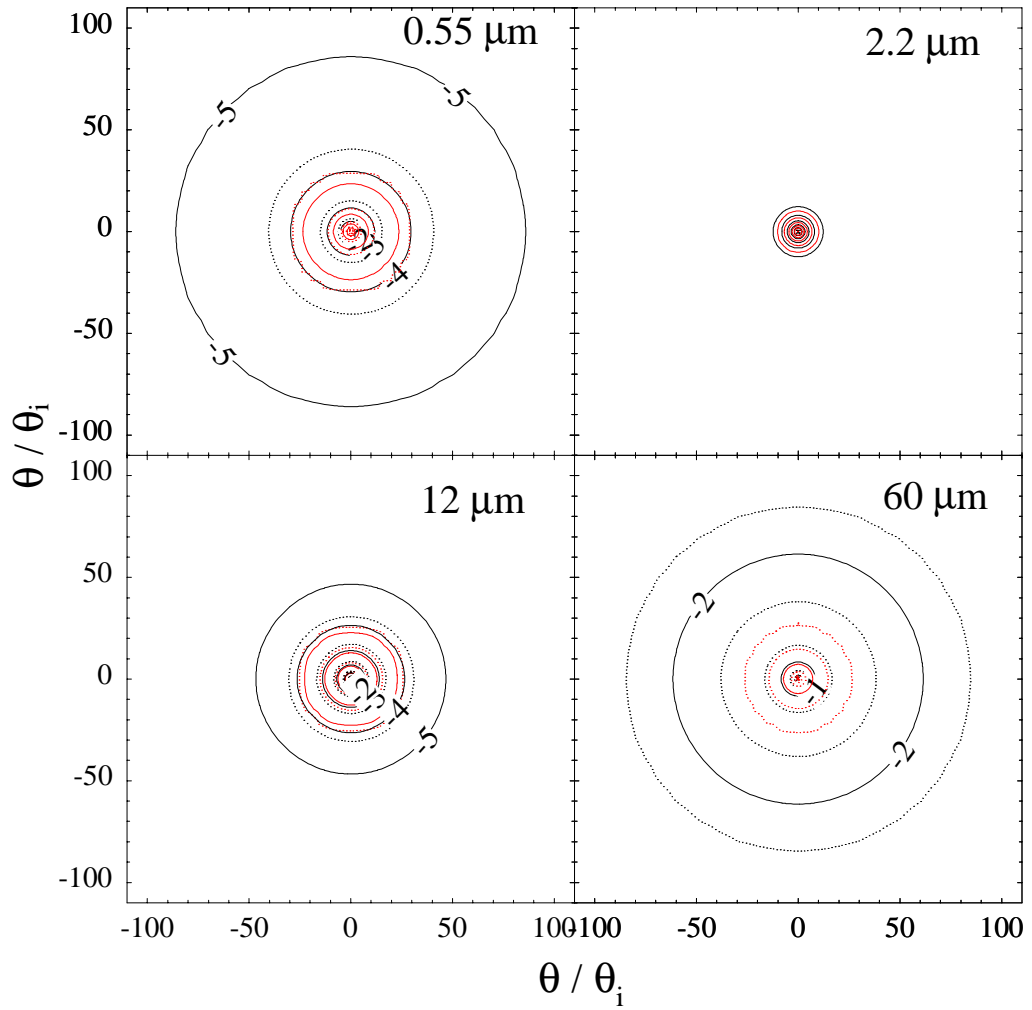
Figure 3.10: Wavelength dependence of surface brightness distribution of a face-on torus. The contours are normalized to the maximum and cover range to 10^{-5} (at 60μm this low level is not reached). Full contour levels are spaced by factors of 10, dotted ones are at half-levels. Results for two torus sizes, $Y = 100$ (black) and $Y = 30$ (red).
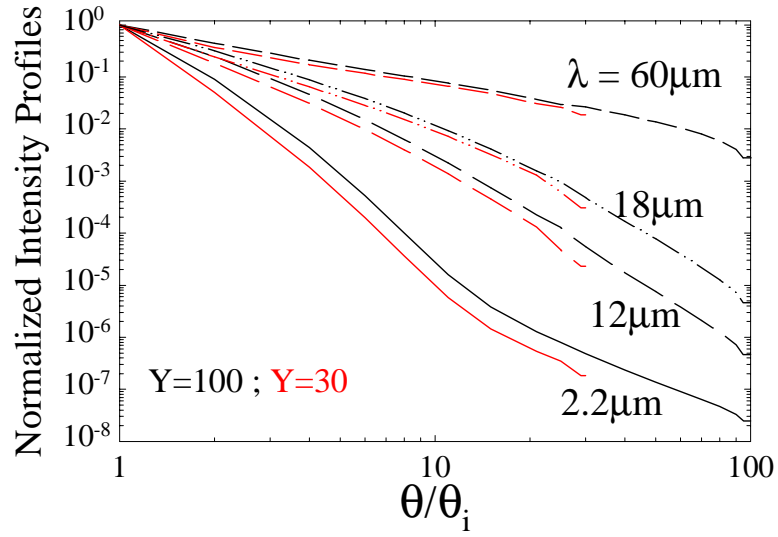
Figure 3.11: Intensity profiles for two torus sizes, $Y = 100$ (black) and $Y = 30$ (red), at the shown wavelengths.
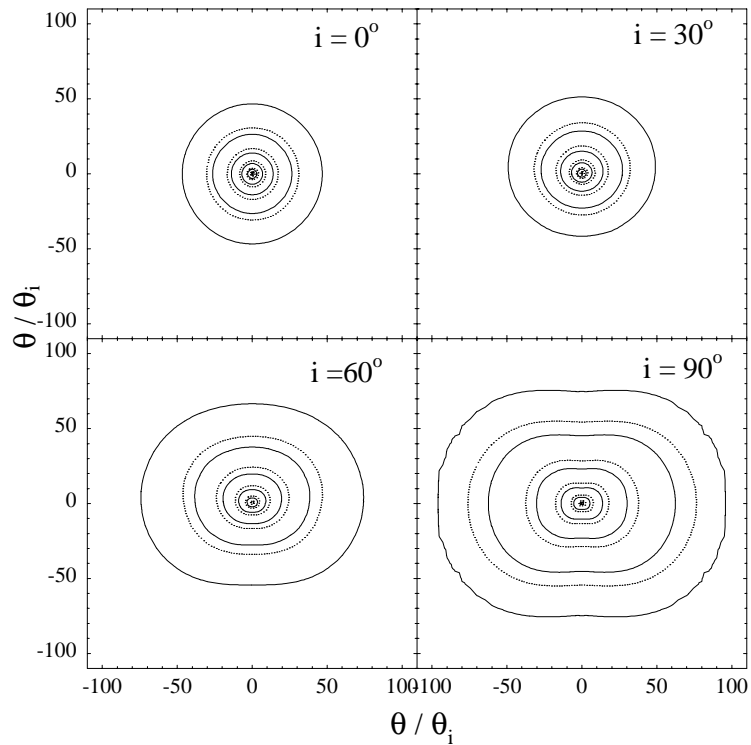
Figure 3.12: Dependence on viewing angle of the surface brightness distribution at $12\mu m$ for a $Y = 100$ torus (Gaussian d.d., $\sigma = 45°$, $\mathcal{N}_{\mathrm{T}} = 5$, $\tau_{\mathrm{V}} = 60$). Normalized to the maximum intensity contours down to level 10^{-5}. Full contour levels are spaced by factors of 10, dotted ones are at half-levels.

putative real one. However, the resolution at longer wavelengths is less than the resolution achieved with shorter wavelengths.

As seen in Fig.3.12, increasing the viewing angle elongates the intensity contours of the models. This is very similar to what is observed for NGC1068 (Bock et al 2000 and Tomono et al 2001). A tentative comparison by eye with their images indicate that NGC1068 seems to be viewed at an angle of 60° or more.
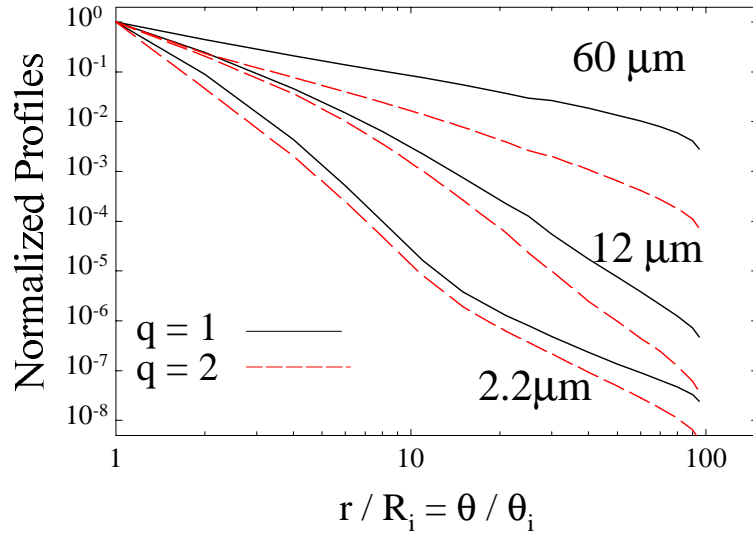
Figure 3.13: Comparison of two radial power laws. Longer wavelengths can better resolve the power of the radial density distribution.

Fig.3.13 shows the intensity profiles for two radial power laws. As expected, intensity decreases faster for steeper radial profiles, because of the corresponding re-distribution of the clouds.

Fig.3.14 shows the intensity profiles at a set of wavelengths for a torus with $Y = 100$. As seen from the plots the torus is the brightest at 12μm. The steeper profiles at shorter NIR wavelengths mean that the size of the torus can be easily underestimated if inferred by observations at these wavelengths.

Observations have limited resolution, the best so far seem to be achieved by Bock et al (2000) and Tomono et al (2001) in the MIR after deconvolution of images of NGC1068. The central core is so far unresolved in the near- and mid-IR (Bock et al (2000)) with a measured FWHM of $0.26''$ (18pc) at 12.5μm. The estimated intrinsic FWHM of the peak is $0.05''$ at 12.5μm to $0.12''$ at 24.5μm.
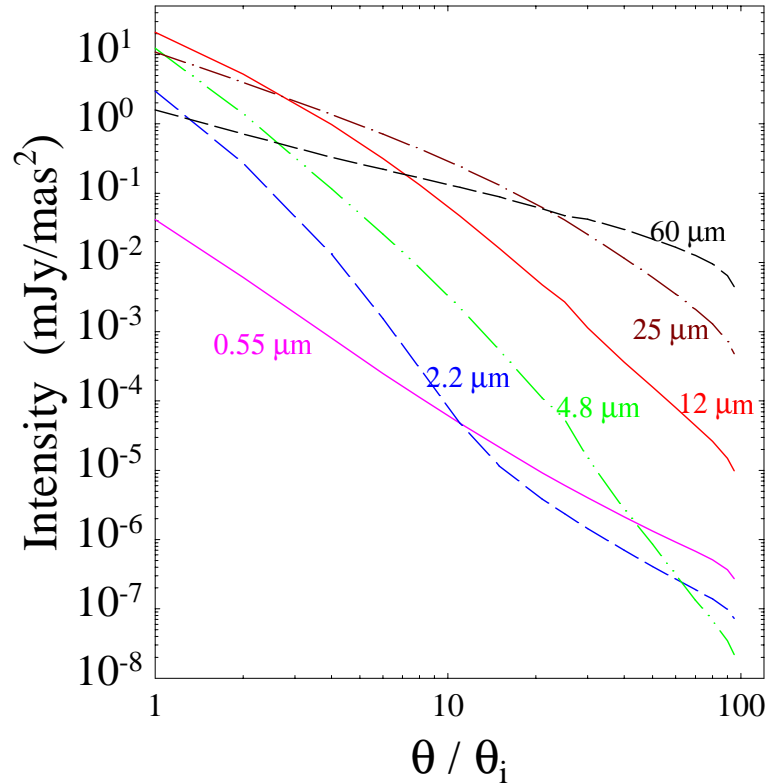
Figure 3.14: Intensity profiles at a set of wavelengths for a torus with $Y = 100$. The torus is the brightest at 12μm. The torus size can be underestimated if the size is inferred only by the NIR brightness profiles.
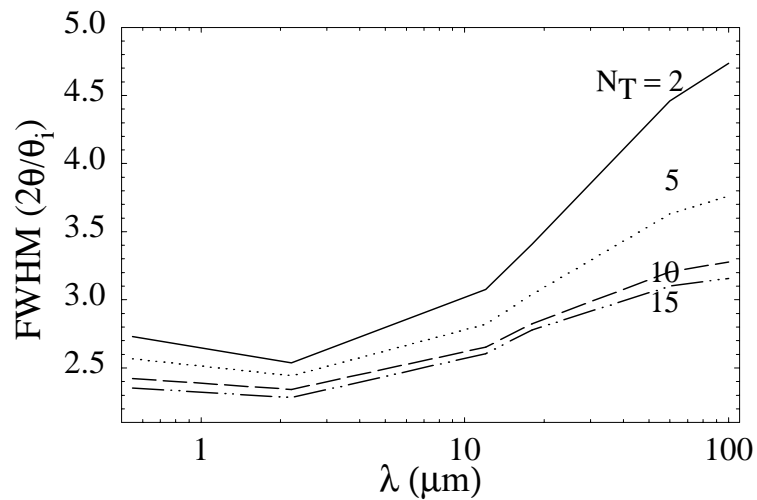
Figure 3.15: FWHM for the shown in Fig.3.14 intensity profiles for a torus with $Y = 100$. $\mathcal{N}_{\mathrm{T}}$ is the model parameter of total number of clouds along the equatorial plane.

For comparison, our models indicate a FWHM of less than 3 pc. Observations by Marco & Alloin (2000) of the same source have a FWHM at 3.5μm and 4.8 μm of less than $0.2''$ (14pc). Marco & Alloin (2000) see evidence for a toroidal structure at $0.5''$ (~ 35pc) from the central peak at an intensity level of 1% of the observed peak brightness, however this wasn't confirmed by the consequent Bock et al (2000) imaging.

Chapter 4

Comparison with Observations

To validate the models of AGN dusty tori one has to compare model results with fluxes from photometric observations. The main problem with this is finding reliable data in the literature, fluxes that are not contaminated by emission from regions, adjacent to the torus, or stars in the host galaxy. Observations of nuclear regions are challenging in principle, because the sources are at distances of the order of Megaparsecs (Mpc) and the typical beam sizes can be $0.1''$ up to $90''$. This makes the size projected on the galaxy of the order of hundreds of parsecs. For comparison, some of the Seyfert galaxies that are nearest to us are at distances of the order of tens of Mpc, so that $1''$ corresponds to 20 - 70 pc, the supposed size of the dusty torus. Therefore, when searching for published data one has to select the smallest possible aperture measurements.

4.1 The 10μm silicate feature

The stretching of the Si-O bond in silicates present in cosmic dust produces a broad feature at 9.7μm, the so called '10 μm feature'. This feature is observed in emission from an optically thin dust and turns into absorption when the optical depth increases. Roche et al (1991) present $8 - 13$ μm spectra of 60 sources, among them two quasars, 16 Sy1 and 12 Sy2 galaxies. The sources chosen for observation were the brightest (at 10μm) examples of their classes. Sy1 and quasars show featureless spectra, with only two Sy1 having a very weak emission feature. Sy2 sources have a shallow absorption feature, with a variety of depths,

with three of the spectra found featureless. Recent ISO observations (Spoon et al 2002) show no silicate emission feature in the average spectrum of 47 continuum dominated (Type 1) AGN.

Homogeneous torus models, in spherical (Granato & Danese 1994) and cylindrical (Pier & Krolik 1992) geometry, produce an emission feature for pole-on views and a deep silicate feature in Type 2 spectra. The depth of the absorption feature is determined by the temperature gradient inside the torus. It is primarily determined by the radial dilution of the radiation ($flux \propto r^{-2}$ in spherical symmetry) and increases with optical depth.
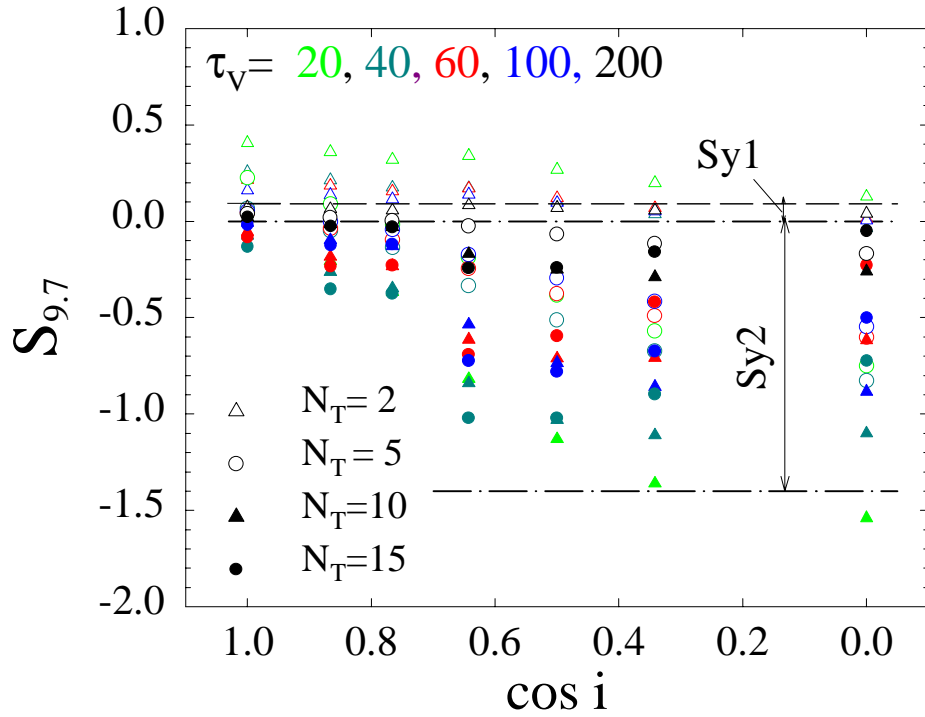
Figure 4.1: Strength of the silicate feature as function of the viewing angle. Single cloud optical depth is color coded; $\mathcal{N}_T$ is represented by symbols. The observed limits of silicate feature strength are shown with horizontal lines.

One of the advantages of a clumpy torus model is that it produces a shallow 10μm silicate absorption feature, in agreement with observations. The reason is that the depth of the feature is limited in a single clump. Single clouds, viewed from their dark side, never show a deep silicate absorption feature (see Fig.2.4). The saturation is a prime result from the almost flat temperature profiles estab-

lished in the clump when the optical depth increases (Fig.6.1). Optical depth is the only parameter of a clump, there is no geometrical factor, unlike the case of a continuous medium. Since the depth of the feature is limited in a single cloud, this is also true for a distribution of clumps. Clouds farther away from the source will be illuminated by the decreasing flux to a lower surface temperature, which will determine the overall shape of single cloud emission. This will additionally modify the appearance of the silicate feature. Its depth, however, will always be limited.

The silicate feature is seen in emission from single clouds, viewed from their hotter, bright sides. Depending on the viewing angle and cloud distribution, these clouds will be obscured to a various extent by the foreground clouds. This is the reason of smearing the feature in a distribution of clouds.

As a measure of the silicate feature strength we adopt the ratio $ln(F_{9.7}/F_c)$ (Pier & Krolik 1992, Granato & Danese 1994), where F_c is the continuum level at the position of the feature (continuum interpolated in $8-13\mu m$). Results for a family of models for a $\sigma = 45°$ Gaussian angular distribution, $q = 1$ power law and torus extent $Y = 30$ are shown in Fig.4.1 with symbols.

The observed ranges of values of the feature strength in Sy1 and Sy2 are shown with straight lines. Instead of a single $S_{9.7} = 0$ line for Sy1 sources, we plotted a narrow range $0 < S_{9.7} < 0.1$, to accommodate the two Sy1 galaxies with observed weak emission features (Roche et al 1991) and to account for the fact that there are still not too many Type 1 sources with observed 8-13μm spectra. The Sy2 spectra according to the same authors, show silicate absorption in the limits of $0 > S_{9.7} > -1.4$.

As seen from Fig.4.1, there are many models that satisfy the requirements of the imposed observational limits. Based on this plot and on inspection of the model spectra (for confirmation) we determine that the emission feature for pole-on view in all models with $\mathcal{N}_T = 2$ is too strong and not consistent with observations.

To comply with the Unified Model we select only those models that show no

42

silicate feature in emission for a face-on viewing angle, and at the same time produce silicate absorption feature for viewing angles $i > 90° - \sigma$ (l.o.s. crossing the denser torus parts).

4.2   Spectral properties of the model spectra

One of the problems in selecting data for comparison is to obtain a complete sample of objects, free from observational bias. Surveys are usually done under some chosen criterion which may introduce a selection bias. The CfA sample of 49 Seyfert galaxies is selected from the fraction of the sky defined either by $\delta \geq 0°$ and $b \geq 40°$ or $\delta \geq -2°.5$ and $b \leq -30°$, and $m_{\mathrm{Zw}} \leq 14.5$ and the galaxies are spectroscopically classified as Sy1 or Sy2 (Huchra & Burg 1992, Osterbrock & Martel 1993). As discussed in Alonso-Herrero et al (2003) this sample may still have a selection bias toward relatively bright objects (Maiolino & Riecke 1995, Ho & Ulvestad 2001). To alleviate this problem Alonso-Herrero et al (2003) add nine more recently re-classified galaxies to the original CfA sample and define an expanded sample of 58 Sy galaxies. The expanded sample includes 33 galaxies optically classified as Sy1.8-2 and 25 galaxies optically classified as Sy1-1.5. Below we compare our model results to these observational data, since we consider them to be a well defined sample of Sy galaxies with non-stellar fluxes.

The spectral characteristics outlined below are widely used as diagnostic and classification tools. Among them the spectral index and colors characterize the shape and slopes of the spectral energy distribution.

4.2.1   Spectral index

Two spectral indices are determined for the models defined as the index required to fit the observed fluxes $f_\nu \propto \nu^{-\alpha}$: α_{opt-IR} in the range of $0.4 - 16\mu$m and α_{IR} in $1 - 16\mu$m. They are compared to the indices determined by Alonso-Herrero et al (2003) for the extended CfA sample of Sy galaxies. A bigger index means steeper spectrum in the shown range. Comparison of model and observational results are shown in Fig.4.2. The Type 2 sources in the sample show a variety of
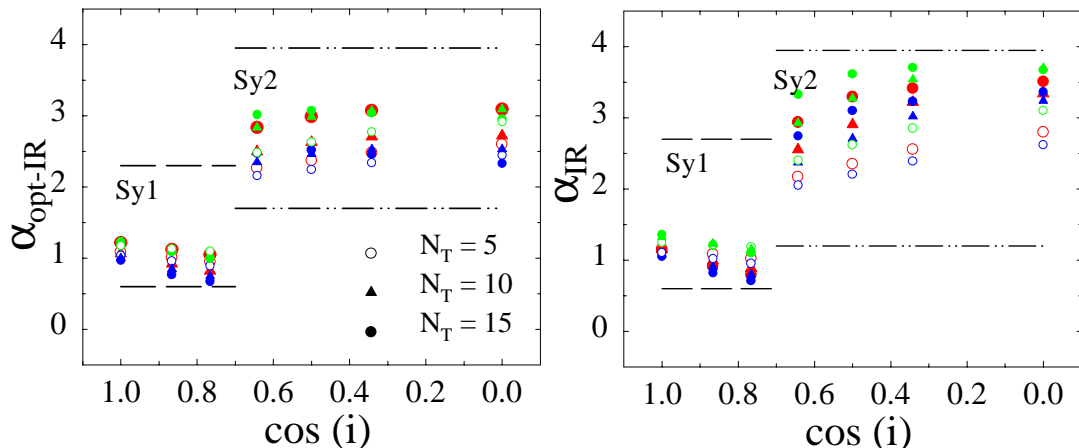
Figure 4.2: Comparison of typical model spectral indices to results of the CfA sample of Sy galaxies. The range of indices for pure Sy1 and Sy2 types are shown with horizontal dashed lines. The models are the same as in Fig.4.1 ($Y = 30$ torus, $q = 1$, Gaussian angular density distribution with $\sigma = 45°$). Single cloud optical depth is color coded as in Fig.4.1 and $\mathcal{N}_T$ is shown in the legend.

spectral indices, none of which is too steep, however. The existing Type 2 models of homogeneous tori produce too steep slopes and have a problem reproducing intermediate slopes with values of 2 to 4. For example, Efstathiou & Rowan-Robinson (1995) models would give slopes for Sy2 from 3 to 8, while the results from the CfA sample (Alonso-Herrero et al 2003) indicate that for the whole sample the highest IR index is 3.8. In models of homogeneous tori the NIR slope increases when increasing the optical depth. In our clumpy torus models, the increase of single cloud optical depth gives a negligible effect, steeper slopes are obtained by increasing the maximum number of clouds $\mathcal{N}_T$. Furthermore, the slopes of our clumpy torus models are in the range of the observed slopes. Alonso-Herrero separates Sy1 and Sy2 based on a slope value $\alpha_{IR} > 1.9$. As seen in Fig.4.2, the separation between the two types of model spectra matches that value.

4.2.2 Colors

Colors are another spectral shape characteristic and are defined as the logarithm of the ratio of emitted flux at two chosen wavelengths. Color-color plots, showing

correlations between two colors are useful way to separate objects with similar types of spectra, revealing underlying physical similarities. We found that a good combination of near-IR colors is [H-L] vs. [L-N], shown in Fig.4.3 for the same sets of models used in Fig.4.1 and Fig.4.2. There is a better separation of the models with this choice of colors compared to other combinations because the chosen wavelengths are sensitive to the spectral slopes where they change the most.
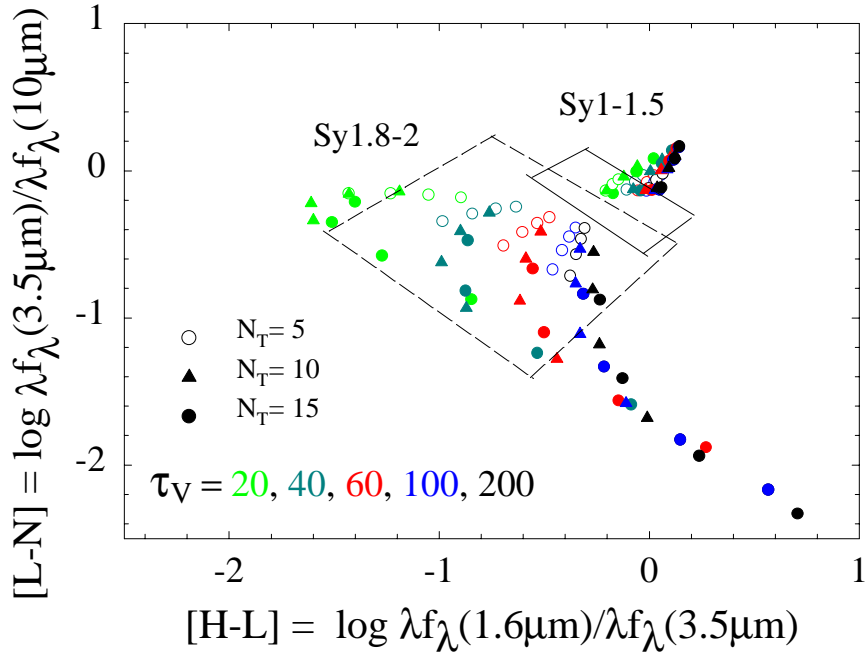
Figure 4.3: Comparison of typical model colors (symbols) to the areas occupied by the CfA sample of Sy galaxies (shown with rectangles). Single cloud optical depth (τ_V) is color coded; $\mathcal{N}_T$ is shown with symbols. Viewing angle increases along tracks for a given $\mathcal{N}_T$.

The colors of galaxies from the CfA sample with data for fluxes at the shown wavelengths were calculated. Some of the data were only upper limit estimates and calculating the colors with them produced large scatter in this graph. There-fore, those sources were not taken into account. The accuracy of the measured photometric fluxes was typically $20 - 30\%$. Areas in the diagram occupied by Sy1-1.5 (9 sources) and Sy1.8-2 galaxies (22 sources), are shown with boxes.

Colors of the same sets of models ($Y = 30, q = 1$, Gaussian angular distribution with $\sigma = 45°$) are shown with symbols, single cloud optical depth is color coded.

It is immediately seen that the models separate in two types: Type 1, in the upper right, which include models for viewing angles $0° - 40°$, and Type 2, with viewing angles $50° - 90°$. Type 1 models group closely, since their spectra, dominated by the AGN continuum, are very similar despite their broad range of parameters. Data occupying the Sy1 box show larger scatter than the models, due to possible additional slight attenuation of the AGN continuum in the ionization cone area. The likelihood of such an additional attenuation is discussed by Alonso-Herrero et al (2003), as well.

Type 2 model results separate a lot more than Type 1 in this color plot, covering most of the of observed Sy2 colors. Limits on possible range of $\mathcal{N}_T$ and τ_V are imposed by the observed range of colors. A torus model is considered to be consistent with the Unified Model if all side-view angles for a given ($\mathcal{N}_T$, τ_V) set of tracks occupy the Sy2 box. As seen from the graph, models with $\mathcal{N}_T \geq 10$ and $\tau_V \geq 100$ go out of the box with increasing the viewing angle. This would imply that all high obscuration sources must be seen at small viewing angles, which is unlikely. Thus, we exclude models in the lower right that are outside the observed color limits, as not compliant with the overall statistics. However, due to the still limited amount of observed sources, there could be sources that can be explained by these high obscuration models, however they would belong more to the exceptions than to the rule.

Based on comparison with the observed colors, the following parameter ranges can be deduced:

- For the lowest possible value of $\tau_V = 20$, $\mathcal{N}_T = 5$ clouds are in the observational limits, with higher $\mathcal{N}_T$ models not too far from them. In view of the observational uncertainties and the lack of too many sources for conclusions with a higher degree of certainty, we consider all $\tau_V = 20$, $\mathcal{N}_T \geq 5$ models to be acceptable.

- Increasing $\mathcal{N}_T$ correlates with reducing the limit for single cloud optical depth. Values of τ_V above 100 for high $\mathcal{N}_T$ cool down further the cloud emission and shift the colors beyond the observed regions. This imposes

upper limits of $\tau_V \sim 60$ for $\mathcal{N}_T = 10$ and $\tau_V \sim 40$ for $\mathcal{N}_T = 15$ models.

4.3 Bolometric flux

The fraction of the bolometric flux that will be received by an observer at distance D, $F_{AGN} = L/4\pi D^2$ is found by integrating the calculated model spectra. Type 1 sources have fractions larger than 1 since an observer will intercept both torus and AGN emission. Higher viewing angles decrease the observed bolometric flux because of increased obscuration. The fraction of the total bolometric flux intercepted by the torus depends on the total number of clouds and single cloud optical depth.

Based on the range of $\mathcal{N}_T$ and τ_V values deduced from the color-color diagram we show $\mathcal{N}_T = 5, \tau_V = 40 - 500$ bolometric flux variation. The values of the observed fractions are from $3 - 8\%$. These model fractions, like those shown
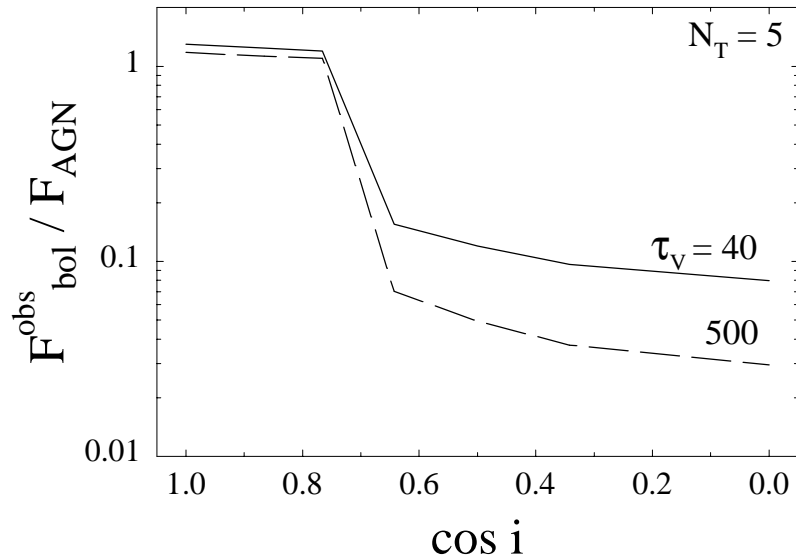
Figure 4.4: Viewing angle dependence of the bolometric flux for models with $Y = 30$, $\mathcal{N}_T = 5$, $\tau_V = 40$ (full line) and $\tau_V = 500$ (dashed).

in Fig.4.4, can be used to infer the actual intrinsic AGN luminosity. This is the main AGN parameter, but it can not be measured in observations directly. From observations in various spectral regions one may get an order of magnitude estimate of the true AGN luminosity. Still this will be a very uncertain number

because of the inherent observational problem – the lack of sufficient resolution of the nuclear region and consequent separation of the contamination from other regions.

Bock et al (2000) observed the nuclear regions of the Sy2 galaxy NGC1068. Their estimate is that the IR luminosity of the central $4''$ area is $1.5 \times 10^{11} L_{\odot}$. The true bolometric AGN luminosity inferred from our models for a $3 - 8\%$ ratio is $(1.9 - 5) \times 10^{12} L_{\odot}$. This is consistent with the putative isotropic AGN luminosity derived in that case to be $\geq 2.5 \times 10^{12} L_{\odot}$.

4.4 Classification of model spectra

To systematize the large database of calculated model spectra, they were processed by code AutoClass (with most recent version Autoclass C 2002, freely available at *http://ic.arc.nasa.gov/ic/projects/bayes-group/autoclass/*). It applies a non-biased, Bayesian statistical approach to look for the best possible classification of the data. This classification code has been used in a wide variety of industrial and scientific applications to reveal underlying patterns and grouping in databases. Applying AutoClass to IRAS data, for example, Ivezić & Elitzur (2000) discovered that different types of galactic objects naturally separate into four classes, and the underlying physical reason for this separation is the object's density distribution.

Without assuming any preliminary conditions on the model data, we supplied to AutoClass all 280 model spectra for a given torus extent of $Y = 30$, radial density power law $q = 1$ and a Gaussian angular distribution with $\sigma = 45°$. The models in the set were for the whole ranges of $\mathcal{N}_{\mathrm{T}}$, τ_{V} and viewing angle. Models that show the silicate emission feature were removed from the sample as they do not correspond to the observations.

AutoClass searches for the most probable separation of models in classes, based on comparison of spectral shapes. Similar spectra will have much higher probability of belonging to one and the same class. Classification is done "blindly" by AutoClass, without any information (e.g., model parameters) other than the spectral shape. The results of grouping of model spectra for $Y = 30$ torus with
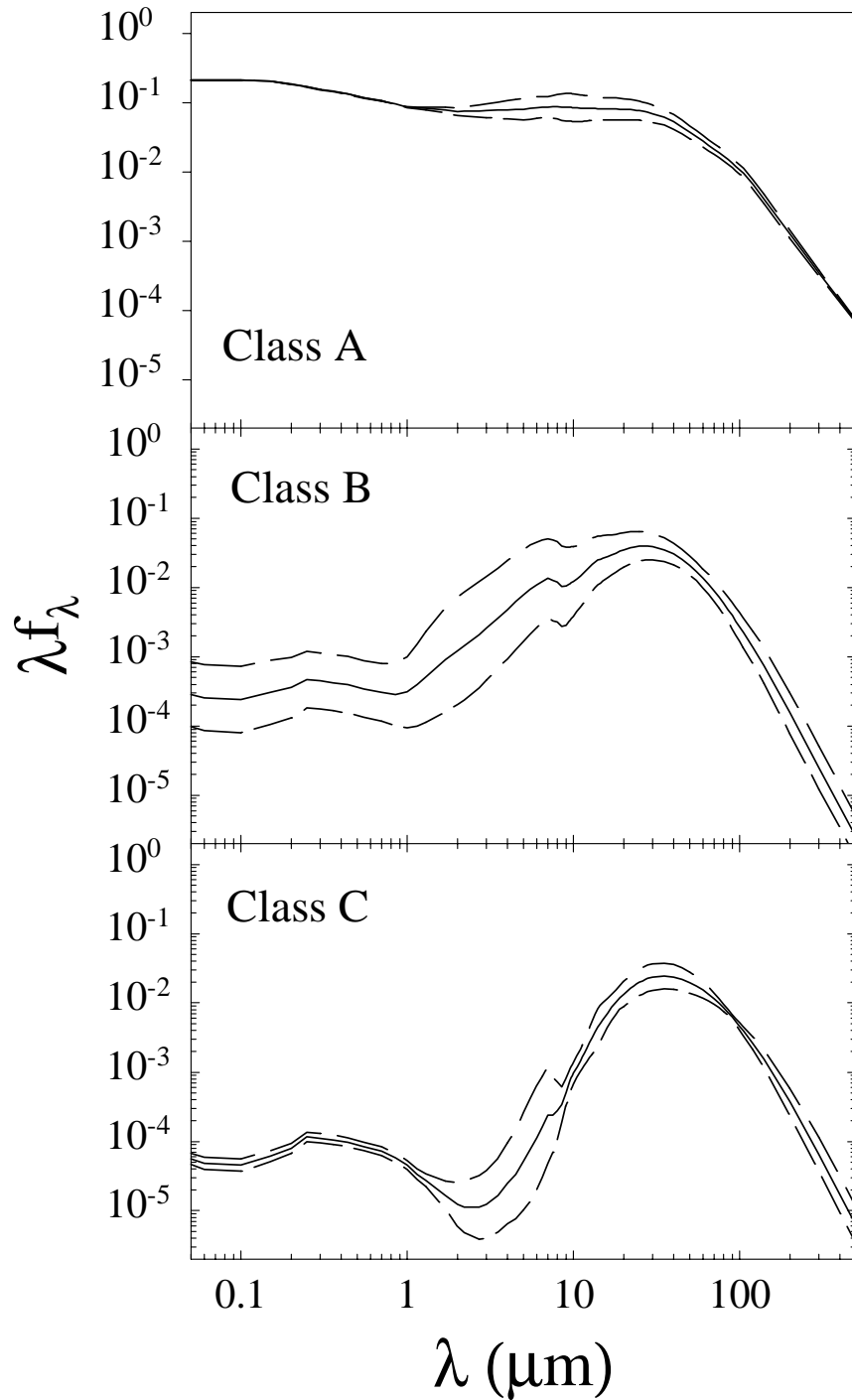
Figure 4.5: Classification of model spectra with the code AutoClass. The models shown here are for a torus extent $Y = 30$, $\sigma = 45°$ Gaussian angular distribution and $q = 1$ radial power law. The mean spectra of each class are shown with full line, dashed lines are ± 1STD deviation from the mean. Class A (43% of the models) corresponds to a typical Type 1 SED; Class B (46% of the models) resembles a typical Type 2 SED; in Class C (11% of the models) are models with extreme values of τ_V and $\mathcal{N}_T$, such spectra are not observed so far.
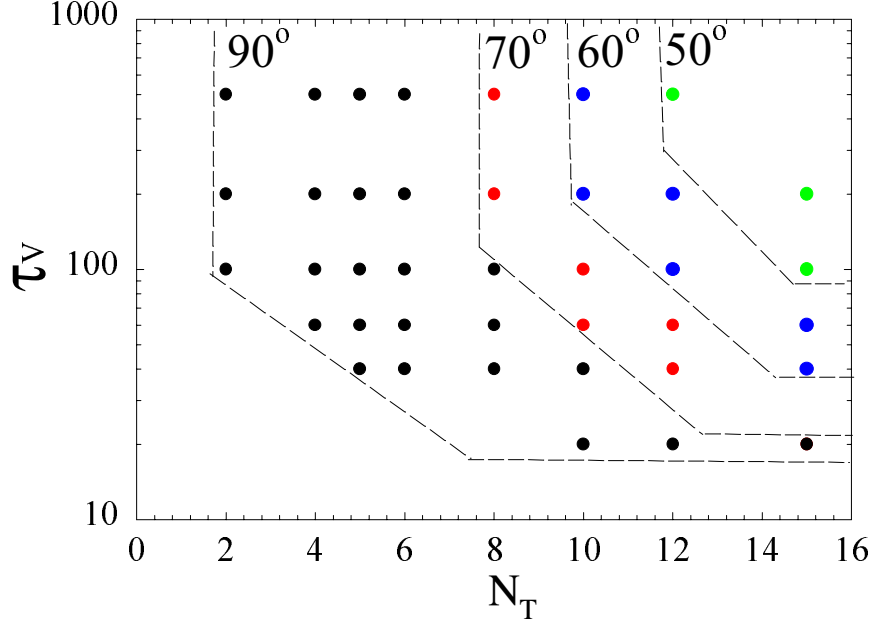
Figure 4.6: Parameter space for Class B spectra (corresponding to typical Type 2 spectra). Models with given $\mathcal{N}_T$ and τ_V will belong to this class if the viewing angle is to the right of the corresponding limits, shown with a dashed line.

$q = 1$ radial power law and a Gaussian angular distribution of clumps, are shown in Fig.4.5. The mean spectra of each class, found by the program, are shown with full lines. 1STD deviations from the mean are shown with dashed lines. AutoClass recognized three classes, denoted with A, B, C.

43% of the models belong to Class A, with a mean spectrum typical for a Type 1 AGN. All values from the parameter space of $\mathcal{N}_T$ and τ_V are included. Based on this classification, one can conclude that Type 1 spectrum can be produced by any value of $\mathcal{N}_T$ and τ_V provided that the viewing angle is $i \leq 90° - \sigma°$ so that the AGN continuum is seen.

46% of the models are grouped in Class B, with an SED resembling a typical Type 2 spectrum. Fig.4.6 gives an idea of the parameter space for Class B models, and, consequently, for the possible range of $\mathcal{N}_T$ and τ_V that may be seen in Type 2 AGN. The dashed lines outline the limits on viewing angle for the given $(\mathcal{N}_T, \tau_V)$ sets that will produce a spectrum belonging to the distribution of Class B spectra. All models with $(\mathcal{N}_T, \tau_V)$ to the right of a given dashed line produce the typical Type 2 spectrum (Class B). This means, for example, that models with very high

50

($\mathcal{N}_T$,τ_V) values, occupying the upper right in the plot, will have spectral shapes in Class B only for viewing angle of 50°. Slightly lower values of $\mathcal{N}_T$ and/or τ_V will make angles up to 60° acceptable. Models in the leftmost region will have Class B spectral shapes for any viewing angle up to 90°.

Class C (11% of the models) contains only models with extreme obscuration: $\mathcal{N}_T \geq 10$, large τ_V, and large viewing angles, $i \geq 70°$. The mean spectral shape of this class is not typical at all for a Type 2 AGN.

4.5   Fits of Type 1 and Type 2 IR spectra

Model fits to the average spectra of quasars (Type 1 sources) are shown with lines in Fig.4.7. There are two lines for each torus size, for the two limiting viewing angles in this case of Type 1 sources, $i = 0°,40°$. As seen the torus size cannot be well constrained with so few observational points. These average spectra indicate that the most likely torus size can be between $Y = 10$ and $Y = 100$. Larger values do not fit that well the data.

In Fig.4.8 the mean Class B spectrum, as obtained from AutoClass, is compared to data for Sy1.8-2.0 galaxies from the CfA catalog. The data are normalized at 16μm and compared with the mean spectrum.

Tentative fits to data for NGC 1068 are shown in Fig.4.9. With an estimated distance of $D = 14.4Mpc$ (cited widely in the literature) NGC1068 is one of the nearest Sy2 galaxies. Nevertheless, there is an inherent uncertainty in the photometric data since the nuclear regions can not be resolved. For this distance $1'' = 70$pc, which is of the order of the torus size. The Adaptive Optics points (Marco & Alloin 2000 and Tomono et al 2001) provide the most likely low flux limit, as a result of their small aperture. The four IRAS wide aperture fluxes are the upper limit in the mid- and far-IR. This Sy2 galaxy is well known to have starburst regions on a kpc scale, so the data beyond $\sim 25\mu$m are most probably contaminated by that. Comparison of fluxes taken with decreasing apertures (LeFloch et al 2001) reveal that the overall MIR flux around 12μm is largely dominated by the AGN. More data are added from Alonso-Herrero et al (2003)
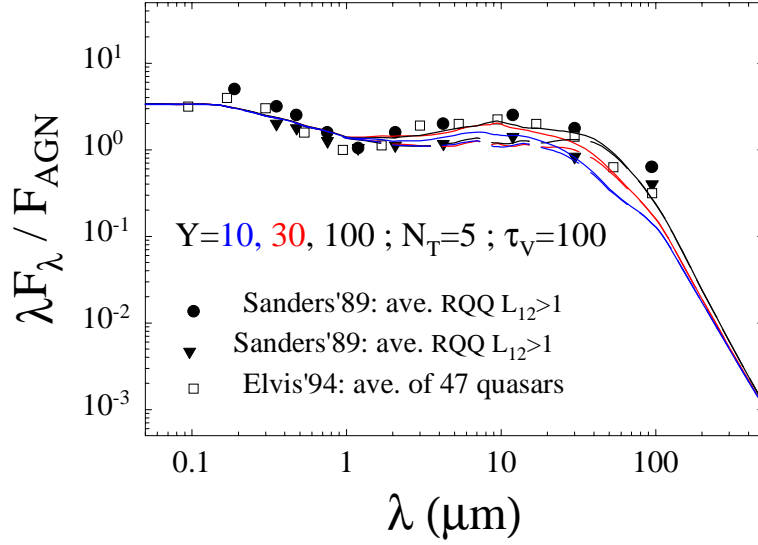
Figure 4.7: Sample model fits to average spectra of quasar samples: Sanders et al (1989) - average of radio-quiet quasars with luminosities $L > 10^{12} L_\odot$ (circles) and $L < 10^{12} L_\odot$ (triangles); mean data of 47 quasars by Elvis et al (1994) (open squares). Data are normalized at 1μm. Models are shown with lines for torus sizes $Y = 10$(blue), $Y = 30$(red) and $Y = 100$(black). All have a Gaussian density distribution with $\sigma = 45°$, radial density power law $q = 1$, single cloud optical depth $\tau_V = 100$, and total number of clouds along equatorial ray $\mathcal{N}_T = 5$.
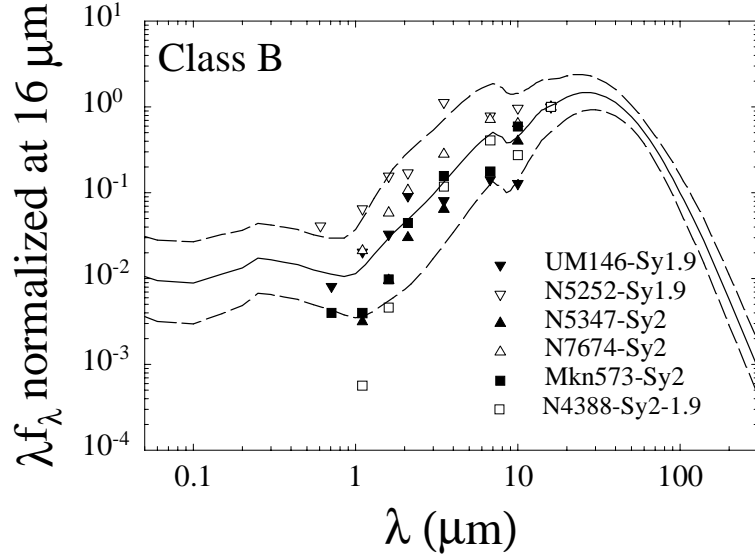
Figure 4.8: The mean Class B spectrum (full line) obtained from AutoClass and ± 1 STD from the mean (dashed). Data from Alonso-Herrero et al (2003) are shown with symbols for six Sy1.8-2.0 galaxies with good quality fluxes. All data are normalized at 16 μm and compared with the mean spectrum.

(shown with filled circles), Rieke & Low (1975) (dots with error bars) and two ISO points (open diamonds) The depth of the silicate feature in the extracted
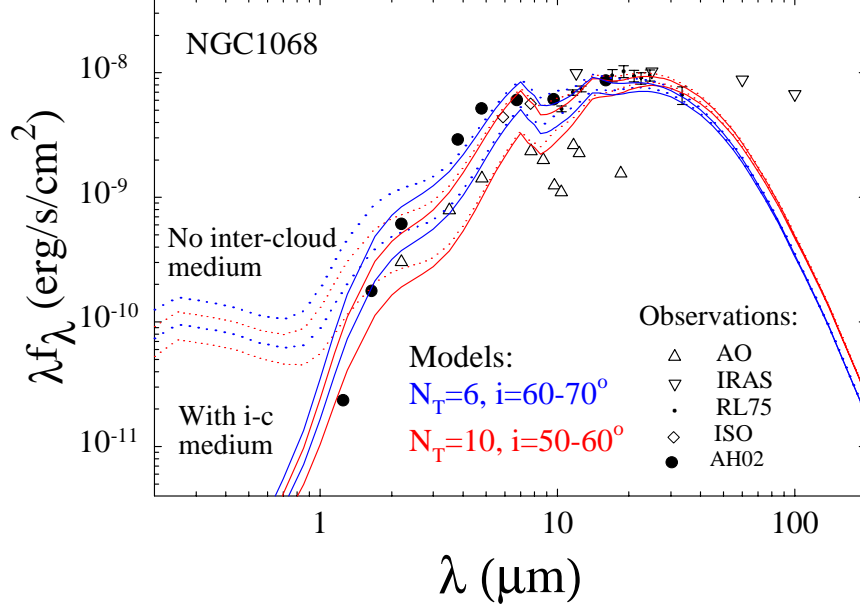
Figure 4.9: Tentative model fits to observational data for NGC1068. Adaptive optics (upward triangles), IRAS(downward triangles), Rieke&Low(1975,dots), ISO(diamonds), Alonso-Herrero (black circles). Blue lines are for a model with $\mathcal{N}_T= 6$, $\tau_V= 100$, $i = 60, 70°$; red lines for $\mathcal{N}_T= 10$, $\tau_V= 100$, $i = 50, 60°$. Full lines are with assumed inter-cloud medium with $\tau_V= 5$ and dotted lines are without it.

nuclear spectrum by LeFloch et al (2001) (5″ aperture, in Fig. 1.1) is less than the one obtained by Bock et al (2000) and Roche et al (1984) with a 4″ aperture. Furthermore, high resolution photometry at the 10μm region taken at various positions of the source (within $50pc$ from the center) reveal completely different profiles. Only the deconvolved profile from the central nuclear region taken with 0.2″ beam resolution shows the absorption feature (Bock et al (2000)). This means that larger apertures data will most likely smear out (or average) the features from such an inhomogeneous environment. Due to the uncertainty of the region around the silicate feature shown in the literature, the spectrum is not added to the data in Fig. 1.1.

In Fig.4.9 are shown models for a torus extent $Y = 30$, $q = 2$ radial density power low, and single cloud optical depth $\tau_V= 100$. The total number of clouds along the equatorial plane can be $\mathcal{N}_T= 6$ with viewing angles $60 - 70°$ (blue lines)

or $\mathcal{N}_\mathrm{T} = 10$ with viewing angles $50 - 60°$ (red lines) .

Our models tend to overestimate the scattered short-wavelength flux ($\lambda \leq 1\mu$m). This is because our single clump emission is based on the averaged slab emission, and slabs will produce the upper limit of scattering from their illuminated sides compared to clouds with more real shapes. On the other hand, presence of an inter-clump medium may bring forward some additional attenuation. Thus a more realistic model may assume an optical depth of this inter-clump medium of a few units ($\tau_\mathrm{V} < 10$, according to estimates of Rowan-Robinson (1995)). Assuming a Galactic type extinction curve, $\tau_\mathrm{V} = 5$ suppresses the shorter wavelengths completely. Reddened model spectra are shown with full lines with corresponding color, not reddened ones are with dotted lines.

Bock et al (2000) estimated that two-thirds of the MIR emission in NGC1068 is the result of re-radiation of the AGN luminosity by a dusty torus viewed at an angle. The observed asymmetry in intensity ratios in two directions of their images were in agreement with a predicted asymmetry from modeling with homogeneous tori (Granato, Danese & Franceschini 1997) viewed at $\sim 65°$. Our tentative fit to observed fluxes is consistent with this estimate of viewing angle.

Our models are for a central source luminosity of $10^{12} L_\odot$ and torus extent $Y = 30 - 100$. The model spectral shapes depend on the temperature distribution while the geometrical sizes relate to luminosity (see eq.(3.1)). The dust sublimation temperature of $1400K$ in our models corresponds to an inner radius of $1pc$. A lower AGN luminosity will decrease the inner radius, corresponding to this dust sublimation temperature, with the same torus extent $Y = R_\mathrm{o}/R_\mathrm{i}$ and same model spectral shapes. This means that a lower luminosity source will have a smaller outer radius R_o of the torus.

Chapter 5

Conclusions

We have built a model of an AGN clumpy torus which successfully explains the observed IR emission. We calculate exactly the emission of directly and indirectly heated clumps. The emission of the medium is described by a source function, which we approximate as a weighted sum of the two types of clouds. The overall emission is obtained by integration over the spatial distribution of clouds.

Individual clouds are considered to have an optical depth of τ_V. They fill a toroidal volume with a radial extent $Y = R_o/R_i$ and a Gaussian angular distribution. Parameters of the cloud distribution are the total number of clouds along an equatorial ray, $\mathcal{N}_T$, and the power of their radial distribution, q.

Our results are in accordance with the Unification Model: the observed two types of AGN spectra are a direct result of viewing angle. Our model of a clumpy torus successfully explains the issues, unresolved by homogeneous tori models: i) the silicate feature appears in absorption for viewing angles intercepting denser torus parts and is smeared out for lines of sight in the opening cone as required by observations; ii) the broad IR bump in the observed AGN spectra is correctly reproduced; iii) the extreme column densities inferred from X-ray observations have a natural explanation with a distribution of optically thick clumps along the line of sight, without resulting in an extremely deep silicate absorption feature in the spectra.

Comparison with observations suggest the following constrains on some of the conditions in AGN dusty tori:

- $\mathcal{N}_{\mathrm{T}} \sim 5 - 10$, single cloud optical depth $\tau_{\mathrm{V}} \geq 40$. When $\mathcal{N}_{\mathrm{T}} < 4$ the 10μm feature appears in emission in pole-on spectra, $\mathcal{N}_{\mathrm{T}} > 10$ shifts the spectrum to longer wavelengths resulting in too little emission in $1 - 10\mu$m and too much emission in the $20 - 100\mu$m range.

- The radial distribution power law appears to be in the range $q = 1 - 2$. $q = 2$ increases the near-IR emission in the spectra on the expense of reduced far-IR parts and vice-versa. Flat density distribution $q = 0$ would give too much FIR emission and does not seem to be supported by observations.

- The cone opening angle is typically $45°\pm15°$and the angular distribution of clouds is likely to be smeared. We find that a generalized Gaussian shape provides a good fit to observations. A torus with sharp cone boundaries is less likely to exist. This estimate for the cone opening angle is in agreement with observational estimates, based on Sy1 and Sy2 number ratios.

- The torus relative size can not be well constrained, it can be $Y = 30$ typically, with $Y = 100$ also quite possible. Higher values are unlikely, due to the excessive far-IR emission of such tori. $Y = 10$ seems to be the lower limit, since it barely provides enough far-IR emission. However, the uncertainty in the observational data, with possible contamination of mid- and far-IR fluxes from regions beyond the torus, does not allow a better estimate. Better observational separation (if possible at all) of the torus contribution to the far-IR emission will make an estimate of the torus extent possible.

The future work will be mostly geared toward fitting the spectra of Type 1 and Type 2 AGN. This will allow constraining the physical conditions in their nuclear environments.

Our model is a single phase model: it considers clumps only in the empty toroidal shape. It seems plausible that an inter-cloud medium exists with a small ($\tau_{\mathrm{V}} \sim$ a few) optical depth. A further development of the model can include this medium into the calculation of the overall torus emission.

Chapter 6

Appendix A: Slab Radiative Transfer

Our model of a single directly illuminated clump is based on the solution for a single plane-parallel dusty slab. Our treatment of this problem follows the formalism developed in Ivezić & Elitzur (1997), which considers the scaling properties of radiative transfer and employs them in solving the radiative transfer problem in a spherically symmetric dusty shell. In the following we present our solution and model results for the case of a plane-parallel geometry.

The transfer of radiation in planar geometry is described by:

$$\mu_i \frac{dI_\lambda}{d\tau} = S_\lambda(\tau_\lambda) - I_\lambda(\tau_\lambda) \tag{6.1}$$

where $S_\lambda(\tau_\lambda)$ is the source function and μ_i is the illumination angle cosine. Because of symmetry the dust density profile is irrelevant, therefore the planar geometry offers the advantage of formulating the radiative transfer problem only in optical depth space. For dust in thermodynamic equilibrium, emitting as a black body at temperature T, and isotropic scattering with albedo ω the source function is $S_\lambda(\tau_\lambda) = (1 - \omega)B_\lambda(T(\tau_\lambda)) + \omega J_\lambda(\tau_\lambda)$, where J_λ is the mean energy density. Integrating the radiative transfer equation (6.1) over angles yields an equation for the angle averaged intensity which is solved coupled with the radiative equilibrium condition at each point of the slab.

Consider a dusty slab with a given optical depth, heated by directional radiation $F_{e,\lambda}\delta(\mu - \mu_i)\delta(\varphi - \varphi_i)$. The angle of illumination $\theta_i = \arccos(\mu_i)$ is measured

in respect to the normal and the azimuthal angle φ_i is arbitrary. The optical depth τ_V across the slab varies from $\tau = 0$ at the illuminated boundary to $\tau = \tau^T$.

Given dust optical properties and total optical depth, the solution is completely determined by the input radiation. Once its spectral shape $f_{e,\lambda}$ is specified, where $F_{e,\lambda} = F_e\,f_{e,\lambda}$, a unique solution is obtained for a given external bolometric flux. The dust is heated by the external radiation and a temperature profile is established across the slab. The surface temperature at normal illumination, T_n, is the highest reached for a given heating flux F_e.

The inverse is also true: prescribing a surface temperature T_n uniquely defines an external bolometric flux F_e. Therefore, the radiative transfer equation (6.1) can be solved imposing one of the two equivalent boundary conditions: either the external bolometric flux F_e or the dust temperature T_n at the illuminated slab surface $\tau_\lambda = 0$. The scale of all radiative quantities is set by the external bolometric flux F_e and scaling them by F_e has the advantage of producing distance independent spectral profiles.

For any slab orientation, the solution of the radiative transfer problem determines the temperature run in the slab and the intensity it emits toward any direction. The emerging intensity from the heated slab $I_\lambda(\theta_i, \theta_o, T_n, \tau_V)$ depends on the illumination angle θ_i, on the observation angle θ_o, on the surface temperature T_n and on the total optical depth of the slab τ_V.

The temperature distribution in the slab is obtained from the radiative equilibrium condition of absorption and emission at any point in the slab: $\int q_{a,\lambda} B_\lambda(T) d\lambda = \int q_{a,\lambda} J_\lambda d\lambda$. Since the mean energy density J_λ is not known beforehand the solution must be found self-consistently. The established temperature profiles depend on illumination angle and optical depth (see Fig.6.1). For optical depths exceeding $\tau_V = 100$ the temperature profiles saturate.

The temperature established at the illuminated boundary is determined by the radiative equilibrium of slab emission and absorption:

$$4q_{a,\lambda}\sigma T_n^4 = F_e q_{ae} \psi(\tau_V, \mu_i) \tag{6.2}$$

where the function $\psi(\tau_V, \mu_i)$ is directly related to the the relative contribution, ϵ,
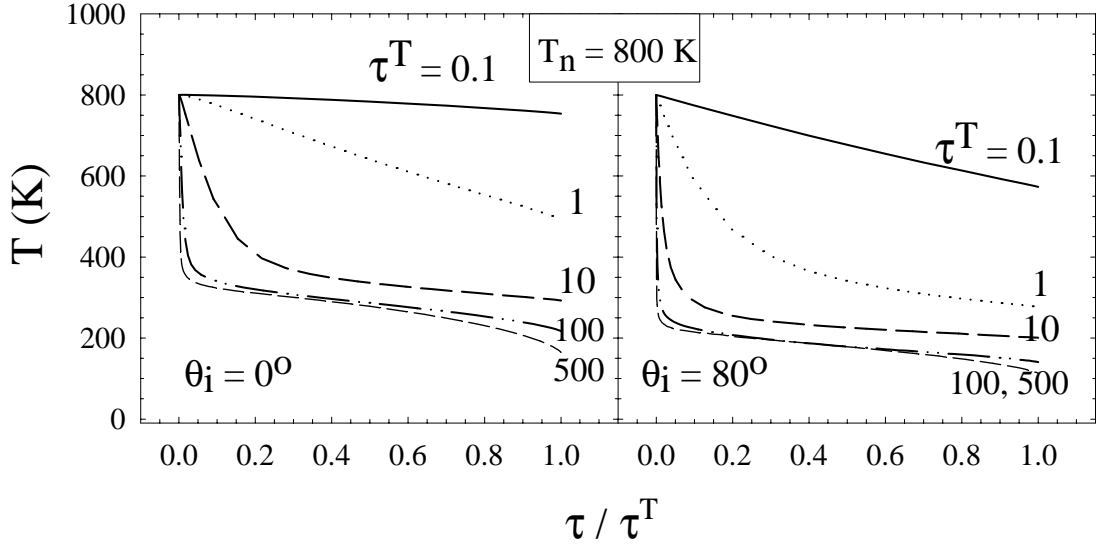
Figure 6.1: Temperature profiles for slabs with $T_n = 800K$ at two illumination angles. For optical depths exceeding τ_V of about 100 the temperature profiles saturate.

of the diffuse radiation at the illuminated boundary

$$\psi = \frac{1}{1-\epsilon}, \qquad \epsilon = \frac{\int q_{a,\lambda} J_\lambda^{\text{diff}}(0)d\lambda}{\int q_{a,\lambda} B_\lambda(T_n)d\lambda} \tag{6.3}$$

At low optical depth the contribution of the diffuse radiation can be neglected and $\psi \to 1$. Ivezić & Elitzur (1997) introduced the function Ψ, which in fact is $\psi\Psi_0$. Its low optical depth value $\Psi_0 = q_{ae}/q_P(T_n)$, equal to the ratio of the spectral averaged absorption efficiencies, contains the temperature dependence. In this respect function ψ is better since it clearly outlines the true dependence of the diffuse radiation (see Fig.6.2).

For a spherical shell this function is not limited from above while in the case of a slab it saturates because of saturation of the diffuse radiation that can be stored in a heated slab. This behavior is a prime result of the different symmetries of a sphere and a slab. While for a spherical shell the diffuse radiation at the inner boundary can reach $\epsilon \sim 1$, in the planar case its value is $\sim 1/2$ the one for sphere. The reason is that the integral over angles in the case of a sphere is over 4π (ea. point of the shell boundary 'sees' all other points, neglecting occultation by the central source), while for a point on the slab surface the angular integration is

over half-space.

As a result of the planar symmetry the contribution of the diffuse radiation will always be finite and will saturate when increasing the slab overall optical depth. This is in contrast to the case of a spherical shell: the diffuse flux at opposite sides of the inner shell boundary cancels, but the diffuse energy density can be indefinitely large. In other words, a spherical shell can store unlimited amount of energy density, while a heated slab can only accommodate a finite amount since it emits from both sides. Another important difference between a spherical and slab
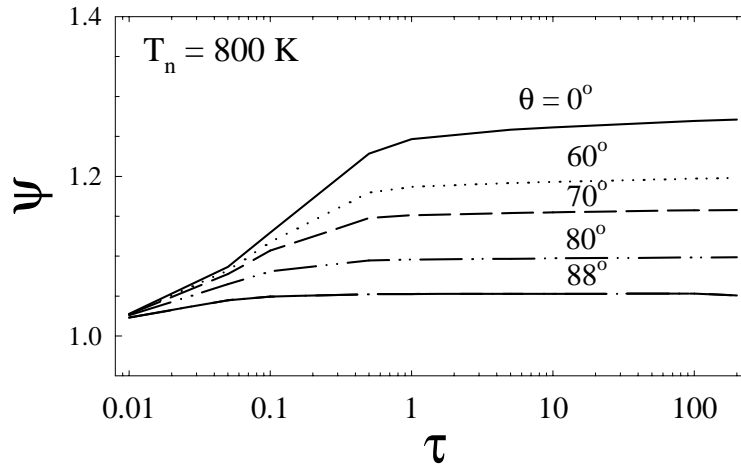
Figure 6.2: The scaling function ψ, calculated for a slab with ISM type dust. It saturates with increasing the slab optical depth and is only weakly dependent on inclination angle.

geometries is the lack of radial dilution in the latter case. This is the main reason for allowing treatment of slab radiative transfer in optical depth space and not in the real space. This is also the reason for appearance of deep silicate absorption feature in the homogeneous torus models.

We have developed the code DUSTY(Ivezić, Nenkova & Elitzur 1999)for continuum radiative transfer, including dust absorption, emission and scattering in spherical or planar symmetry. With DUSTY we calculated the intensity emitted by a dusty slab with given dust spectral properties and specified overall optical depth. The dust is assumed to have a standard Galactic composition of graphite and silicates (Draine & Lee 1984). The grains are considered spherical with MRN

(Mathis, Rumpl & Nordsieck 1977) size distribution. Given their optical constants (n, k) the absorption and scattering cross-sections are calculated in DUSTY by means of the Mie theory.

The slab is heated by external radiation with a prescribed spectral profile and illumination angle. We chose a typical AGN spectral shape, $\lambda f_\lambda = $ constant in the wavelength range 0.01-0.1 μm and $\propto \lambda^{-0.5}$ for 0.1-100 μm (see, e.g., Pier & Krolik 1992, Laor & Draine 1993).

The optical depth across the slab thickness at wavelength λ is $\tau_\lambda = q_\lambda \tau_V$ where τ_V is the optical depth at the visual and q_λ is the proper efficiency factor of standard interstellar dust. With AGN luminosity $L_{12} = L/10^{12} L_\odot$, the bolometric flux illuminating a slab at distance r is $F_e = L/4\pi r^2$. In Fig.6.3 are shown emerg-
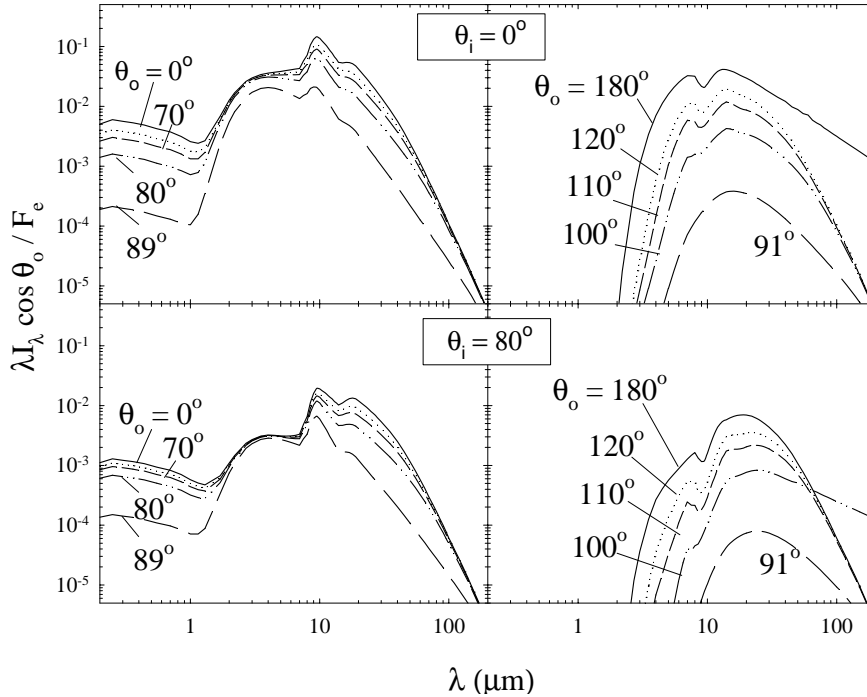
Figure 6.3: Emerging intensities from each side of a slab of ISM dust with a surface temperature $T_n = 800K$ and optical depth $\tau_V = 100$ ($\tau_{10} \sim 5$). The illumination and observation angles θ_i and θ_o are measured in respect to the normal at the illuminated side. The 10μm feature is seen in emission in spectra from the illuminated side (left panels); the feature appears in absorption in spectra from the dark side (right panels).

ing intensity spectral shapes. The panels on the left show the intensity from the illuminated side, the right panels are spectra from the other, dark side. For each

of the two illumination angles are shown results for a set of observational angles. A large optical depth is chosen in order to emphasize the differences between spectra from each slab side. As seen from Figs.6.3 and 6.4 the silicate feature always

Figure 6.4: Emerging intensities from slabs at $T_n = 800K$ with increasing optical depth. Normal illumination ($\theta_i = 0°$) and observation angle $\theta_o = 10°, 170°$ respectively, for left and right panel. Note the decrease in contrast of the $10\mu m$ feature in the spectra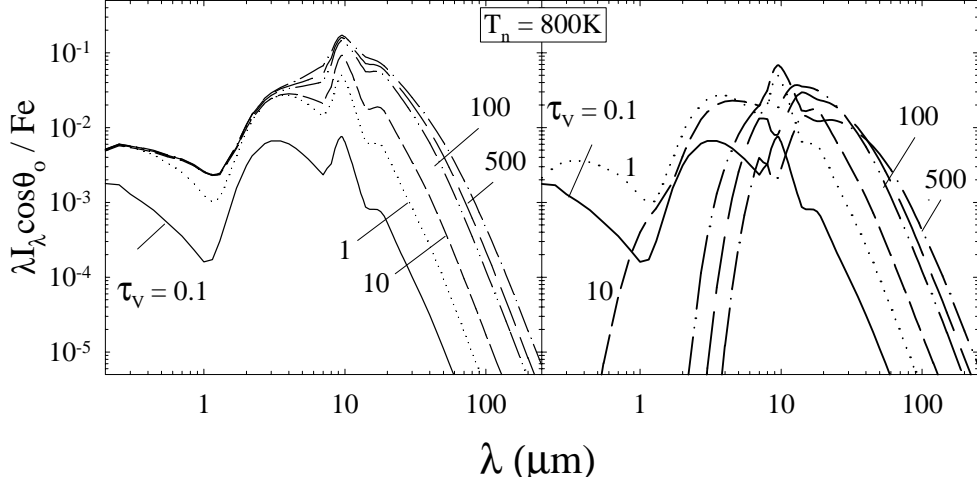 from the illuminated side with increasing optical depth and the developing of an absorption feature in the spectra from the dark side.

appears in emission in spectra from the illuminated slab side while it is seen in absorption at large ($\tau_V \geq 20$) optical depths in spectra from the dark slab side. Increasing the illumination angle sharpens the feature to some extent for observation angles $\theta_o \leq 60°$ while increasing the observation angle decreases its strength at a fixed θ_i. Increasing the illumination angle reduces the radiation flux heating the slab, the slab emission cools down and the resultant spectra are affected in a way similar to increased optical depth. The spectral shapes are a prime result of the dust temperature profile established across the slab (see Fig.6.1). When viewed from the dark side the cooler dust in front of the warmer one creates an absorption feature (and inversely for spectra from the bright slab side). The absorption feature is sharper when the temperature gradient is stronger, as a result of increased total optical depth or increased illumination angle. Note the saturation of the temperature profiles when increasing the optical depth beyond $\tau_V \sim 100$. This means that the spectral properties will not change noticeably when

the slab optical depth increases above this value. The reason for saturation of the temperature profiles across a slab is the exponential attenuation of the external heating radiation when it propagates inside the slab. Increasing the total optical depth shortens the penetration depth which means that the temperature profile is totally determined by diffuse radiation. And saturation of the diffuse radiation is one of the specifics of dusty slabs. Fig. 6.5 shows the effect of decreasing surface
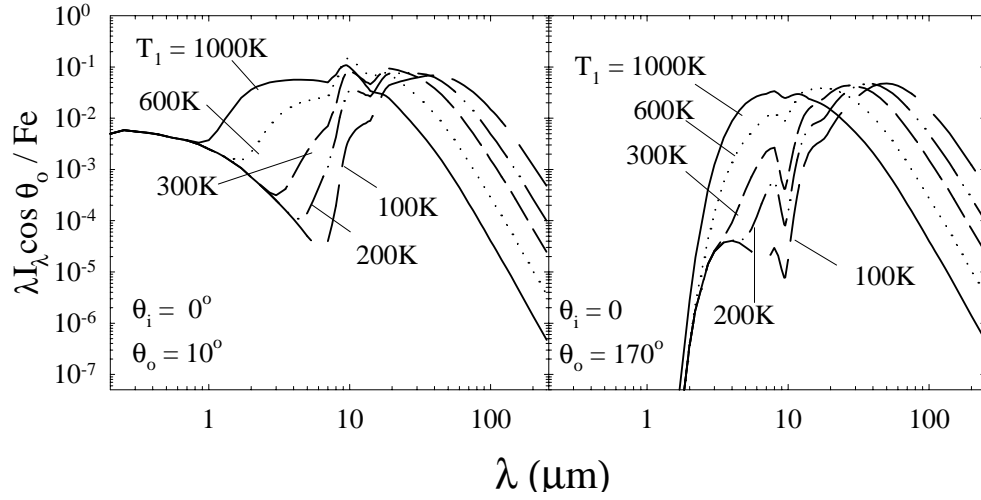
Figure 6.5: Same as Fig. 6.3 but for decreasing surface temperatures: $\tau_V = 100$; normal illumination. The 10μm silicate feature in the spectra from the illuminated slab side gradually vanishes due to the overall shift of the low temperature slab emission to longer wavelengths. The feature appears in absorption in the spectra from the dark side.

temperature on the 10μm silicate feature. At lower temperatures the overall slab emission shifts towards longer wavelengths. Since the silicate emission feature in the spectral profiles from the slab bright side appears upon the dust continuum emission, when the dust is cooler than about $300K$ (the temperature corresponding roughly to 10μm) the feature contrast decreases. At surface temperature of $100K$ the feature disappears completely in the spectra from the illuminated slab side.

Chapter 7

Appendix B: The Radiative Transfer Code DUSTY

● **Solution method**

We have developed the publicly available code DUSTY (Ivezić, Nenkova & Elitzur 1999, Nenkova, Ivezić & Elitzur 2000) for continuum radiative transfer in spherical or planar geometry. DUSTY utilizes the scaling properties of the radiative transfer problem, which are discussed in depth by Ivezić & Elitzur (1997). The code solves the integral equation for the energy density obtained from the formal solution of the radiative transfer equation. The equation, including diffuse emission and scattering, is coupled with the condition of radiative balance at any point of the dusty medium. We have employed a direct solution method, i.e., the numerical integration over angles and optical depth is transformed into multiplication with a matrix of weight factors (Schmidt-Burgk 1975). The matrix is determined purely by the geometry and is calculated only once for each radiative moment on a given spatial grid. The energy density and flux at every point are then determined by matrix inversion.

That gives our method an edge in speed over other schemes. The employed direct method of solution provides fast and stable convergence even for optical depths as large as $\tau_V \sim 1000$. The radiative transfer problem in spherical symmetry is solved on grids for dimensionless radius and impact parameter, whereas for the plane-parallel case the calculation is performed in optical depth space.

- **Analytical expressions**

Code versions after the official 1999 release $\mathsf{DUSTY}2.01$ allow input of a boundary condition either the dust condensation temperature T_1, or the external bolometric flux at the boundary, F_e. The latter can be entered in one of the three equivalent ways: i) the flux itself; ii)luminosity, distance; iii)the effective temperature corresponding to the external bolometric flux, $T_e = (F_e/\sigma)^{0.25}$.

We solve the integral equation for the mean energy density $(J = \int I d\Omega / 4\pi)$. In spherical geometry it is

$$J_\lambda(y) = \frac{F_e}{4\pi y^2} f_{e,\lambda} e^{-\tau_\lambda(y)} + \frac{1}{2} \int \int S_\lambda(y') e^{\tau_\lambda(y',\mu) - \tau_\lambda(y,\mu)} d\tau_\lambda(y',\mu) d\mu \qquad (7.1)$$

In plane-parallel geometry with directional illumination $I_{e,\lambda} \delta(\mu - \mu_1) \delta(\phi - \phi_1)$ at an angle $\arccos \mu_1$ in respect to the normal and arbitrary azimuthal angle ϕ_1,

$$J_\lambda(\tau_\lambda) = \frac{1}{4\pi} I_{e,\lambda} e^{-\tau_\lambda/\mu_1} + \frac{1}{2} \int_0^{\tau^T} S_\lambda(t) E_1 |\tau_\lambda - t| dt \qquad (7.2)$$

Introducing the spectral shape $f_{e,\lambda}$, the flux illuminating the slab is

$$F_e f_{e,\lambda} = \int \mu I_{e,\lambda} \delta(\mu - \mu_1) \delta(\phi - \phi_1) d\mu d\phi = \mu_1 I_{e,\lambda} = \mu_1 I_e f_{e,\lambda}$$

The source function includes dust emission and isotropic scattering,

$$S_\lambda = (1 - \omega_\lambda) B_\lambda(T) + \omega_\lambda J_\lambda \qquad (7.3)$$

The temperature at each point of the dusty shell (or slab) is determined from the radiative equilibrium of dust emission and absorption:

$$\int q_{a,\lambda} B_\lambda(T) d\lambda = \int q_{a,\lambda} J_\lambda d\lambda \qquad (7.4)$$

The mean intensity in DUSTY , u_λ , is scaled by the external bolometric flux and the radial dilution factor in spherical symmetry is accounted for:

$$u_\lambda(y) = \frac{4\pi y^2}{F_e} J_\lambda(y) = \frac{4\pi y^2}{\sigma T_e^4} J_\lambda(y) \qquad (7.5)$$

The analogous expression for slab is

$$u_\lambda(\tau_\lambda) = \frac{4\pi}{F_e} J_\lambda(\tau_\lambda) = \frac{4\pi}{\sigma T_e^4} J_\lambda(\tau_\lambda) \qquad (7.6)$$

Thus, the integral equation we solve in spherical geometry is:

$$u_\lambda(y) = f_{e,\lambda}e^{-\tau_\lambda(y)} + \frac{1}{2}\int\int s_\lambda(y')\left(\frac{y}{y'}\right)^2 e^{\tau_\lambda(y',\mu)-\tau_\lambda(y,\mu)}d\tau_\lambda(y',\mu)d\mu$$

$$s_\lambda(y') = 4(1-\omega_\lambda)y'^2\left(\frac{T(y')}{T_e}\right)^4 b_\lambda\left(T(y')\right) + \omega_\lambda u_\lambda(y') \tag{7.7}$$

along with the scaled radiative equilibrium condition (7.4):

$$T^4\int q_{a,\lambda}b_\lambda(T)d\lambda = \frac{T_e^4}{4\,y^2}\int q_{a,\lambda}u_\lambda(y)d\lambda \tag{7.8}$$

Here $b_\lambda(T) = (\pi/\sigma T^4)B_\lambda(T)$ and $q_{aP}(\mathrm{T})= \int q_{a,\lambda}b_\lambda(T)d\lambda$. (7.8) yields the equation for dust temperature, written in the form $f_1(y) - f_2(y)g(T) = 0$:

$$\int q_{a,\lambda}u_\lambda(y)d\lambda - \left(\frac{4\,y^2}{T_e^4}\right)q_{aP}(T)T^4 = 0 \tag{7.9}$$

The definition of Ψ is the same as before (Ivezić & Elitzur 1997),

$$\Psi = \frac{4\sigma T_1^4}{F_e} = 4\left(\frac{T_1}{T_e}\right)^4$$

Introduction of the effective temperature makes clear that the the two ways of specifying boundary condition are equivalent and symmetric. When input is the external bolometric flux in some form the effective temperature T_e is known and DUSTY finds the surface temperature as the first element of the temperature array. When dust sublimation temperature T_1 is given in input, T_e is determined from the radiative equilibrium condition at the first grid point $iY = 1$ only:

$$T_e^4 = T_1^4\frac{4\,q_{aP}(T_1)}{\int q_{a,\lambda}u_\lambda(1)d\lambda} \tag{7.10}$$

The analogous expressions in case of slab, directionally illuminated at an angle μ_1 are:

$$u_\lambda(\tau_\lambda) = \frac{1}{\mu_1}f_{e,\lambda}e^{-\tau_\lambda/\mu_1} + \frac{1}{2}\int_0^{\tau_T}s_\lambda(t)E_1|\tau_\lambda - t|dt$$

$$s_\lambda(t) = 4(1-\omega_\lambda)\left(\frac{T(t)}{T_e}\right)^4 b_\lambda\left(T(t)\right) + \omega_\lambda u_\lambda(t) \tag{7.11}$$

the scaled flux $f_\lambda = F_\lambda/F_e$ in the slab is

$$f_\lambda(\tau_\lambda) = f_{e,\lambda}e^{-\tau_\lambda/\mu_1}$$
$$+ \frac{1}{2}\left[\int_0^{\tau}s_\lambda(t)E_2|\tau_\lambda - t|dt - \int_\tau^{\tau_T}s_\lambda(t)E_2|\tau_\lambda - t|dt\right] \tag{7.12}$$

66

and the scaled radiative equilibrium condition (7.4):

$$T^4 q_{aP}(T(t)) = \frac{T_e^4}{4} \int q_{a,\lambda} u_\lambda(t) d\lambda \qquad (7.13)$$

Thus the equation $f_1(y) - f_2(y)g(T) = 0$ for the case of slab is:

$$\int q_{a,\lambda} u_\lambda(y) d\lambda - \frac{4}{T_e^4} q_{aP}(T) T^4 = 0 \qquad (7.14)$$

- **The algorithm**

The integral equation for the energy density can be written formally, introducing integral operators of dust emission and scattering. For spherical case they are respectively

$$\hat{O}^{em} = \frac{(1 - \omega_\lambda)}{2} \int 4y'^2 \left(\frac{T}{T_e}\right)^4 b_\lambda(T) e^{\tau_\lambda(y',\mu) - \tau_\lambda(y,\mu)} \left(\frac{y}{y'}\right)^2 d\tau_\lambda(y',\mu) d\mu$$

and

$$\hat{O}^{sca} = \frac{\omega_\lambda}{2} \int e^{\tau_\lambda(y',\mu) - \tau_\lambda(y,\mu)} \left(\frac{y}{y'}\right)^2 d\tau_\lambda(y',\mu) d\mu$$

In the planar case they are

$$\hat{O}^{em} = \frac{(1 - \omega_\lambda)}{2} \int 4 \left(\frac{T}{T_e}\right)^4 b_\lambda(T) E_1 |\tau_\lambda - \tau_\lambda'| d\tau_\lambda'$$

and

$$\hat{O}^{sca} = \frac{\omega_\lambda}{2} \int E_1 |\tau_\lambda - \tau_\lambda'| d\tau_\lambda'$$

In this notation the equation solved in DUSTY has the form:

$$\left[\hat{1} - \hat{O}^{sca}\right] * u_\lambda = f_{e,\lambda} e^{-\tau_\lambda} + \hat{O}^{em}(T) \qquad (7.15)$$

Therefore, the problem of solving the integral equation for the energy density reduces to solving the matrix equation:

$$\tilde{A} * u_\lambda = \tilde{B} + \tilde{C}(T) \qquad (7.16)$$

and the energy density vector $u_\lambda(\text{y})$ is found by matrix inversion.

- **Code capabilities**

DUSTY is written in standard FORTRAN-77 and has been tested on a variety of platforms. One of the advantages of the code is the flexible, user-friendly input / output interface, which explains its popularity and wide use among the astronomical community. An important advantage of the code is that the number of independent input model parameters is minimal since it fully utilizes the scaling properties of the radiative transfer.

The input contains three types of data: physical parameters, numerical accuracy parameters, and flags for optional output files. The physical parameters include characteristics of the external radiation, properties of the dust grains, and the envelope density distribution.

The code is publicly available for various modeling purposes. Details and instructions about the many options can be found in DUSTY's Manual (Ivezić, Nenkova & Elitzur 1999).

Bibliography

Aitken, D. and Roche P., 1985, MNRAS, 213, 777

Akiyama, M., Ueda, Y. and Ohta, K., 2002, ApJ, 567, 42

Alexander, D.M., Efstathiou, A., Hough, J.H., Aitken, D.K., Lutz, D., Roche, P.F. and Sturm, E., 1999, MNRAS, 310, 78

Alloin, D., Pantin, E., Lagage, P.O. and Granato,G.L., 2000, A&A, 363, 926

Alonso-Herrero, A., Ward, M. and Kotilainen, J.K., 1997, MNRAS, 288, 977

Alonso-Herrero, A., Quillen, A., Simpson, Ch., Efstathiou, A. and Ward, M., 2001, AJ, 121, 1369

Alonso-Herrero, A., Quillen, A., Rieke, G., Ivanov, V. and Efstathiou, A., 2003, in press

Andreani, P., Franceschini, A. and Granato, G.L. , 1999, MNRAS, 306, 161

Antonucci, R.R.J., 1993, ARA&A, 31, 473 (Ant93)

Antonucci, R.R.J. and Miller, J.S., 1985, ApJ, 297, 621 (AM85)

Bayesian classification code Autoclass C, available at *http://ic.arc.nasa.gov/ic/projects/bayes-group/autoclass/*

Barvainis, R., 1987, ApJ, 320, 537

Bassani L., Dadina, M., Maiolino, R., Salvati, M., Risaliti, G., Della Ceca R., Matt, G. and Zamorani G., 1999, ApJS, 121, 473

Bianchi S., Ferrara, A., Davies, J. I. and Alton, P. B., 2000, MNRAS, 311, 601

Bock, J.J., Marsh, K.A., Ressler, M.E. and Werner, M.W. 2000, AJ, 120, 2904

Chandrasekhar, S., 1953, Radiative Transfer, Oxford Univ.Press

Clavel, J., Schulz, B., Altieri, B., Barr, P., Claes, P., Heras, A., Leech, K., Metcalfe, L., and Salama, A., 2000, A&A, 357, 839

Draine, B.T. and Lee, H.M., 1984, ApJ, 285, 89

Efstathiou, A. and Rowan-Robinson, M., 1995, MNRAS 273, 649

Elvis, M., Wilkes, B. J., McDowell, J. C., Green, R. F., Bechtold, J., Willner, S. P., Oey, M. S., Polomski, E. and Cutri, R., 1994, ApJS, 95, 1

Fadda, D., Giuricin, G., Granato, L. and Vecchies, D., 1998, ApJ, 496, 117

Franceschini, A., Bassani, L., Cappi, M., Granato, G. L., Malaguti, G., Palazzi, E. and Persic, M., 2000, A&A, 353, 910

Franceschini, A., Braito, V. and Fadda, D., 2002, MNRAS, 335, 51

Galliano, E. and Alloin, D., 2002, A&A, 393, 43

Gallimore, J. F., Baum, S. A. and O'Dea, C. P., 1997, Nature, 388, 852

Granato, G.L. and Danese, L., 1994, MNRAS, 268, 235

Granato, G.L., Danese, L. and Franceschini, A., 1997, ApJ, 486, 147

Guainazzi M., Fiore, F., Matt, G. and Perola G.C., 2001, MNRAS, 327, 323

Ho, L. and Ulvestad, J., 2001, ApJ, 133, 77

Huchra, J., and Burg, R., 1992, ApJ, 393, 90

Imanishi M. and Ueno, S., 2000, ApJ, 535, 626

Ivezić, Ž. and Elitzur, M., 1997, MNRAS 287, 799 (IE97)

Ivezić, Ž. and Elitzur, M., 2000, ApJ 534, L93

Ivezić,Ž., Nenkova, M. and Elitzur, M., 1999, User Manual for DUSTY, Internal Report, Univ. of Kentucky, *http://www.pa.uky.edu/∼moshe/dusty/*

Jaffe, W., Ford, H.C., Ferrarese, L., van den Bosch, F. and O'Connell, R.W., 1993, Nature, 364, 213

Krolik, J., 1999, Active Galactive Nuclei, Princeton: Princeton University Press

Krolik, J. and Begelman, M., 1986, ApJ, 308, L55

Krolik, J. and Begelman, M., 1988, ApJ, 329, 702

Laor, A. and Draine, B.T., 1993, ApJ, 402, 441

Lawrence, A., 1987, PASP, 99, 309-334

Le Floc'h, E., Mirabel, I. F., Laurent, O., Charmandaris, V.,Gallais, P., Sauvage, M., Vigroux, L., and Cesarsky, C., 2001, A&A, 367, 487

Loska, Z., Szczerba, R. and Czerny, B., 1993, MNRAS, 261, 63L

Maiolino, R. and Rieke, G., 1995, ApJ, 454, 95

Maiolino, R., Marconi, A., Salvati, M., Risality, G., Severgnini, P., Oliva, E., La Franca, F., and Vanzi, L., 2001, A&A, 365, 28

Maiolino, R., Marconi, A. and Oliva, E., 2001, A&A, 365, 37

Manske, V., Henning, Th. and Men'shchikov, A. B., 1998, A&A, 331, 52

Mathis J.S., Rumpl W. and Nordsieck K.H., 1977, ApJ, 217, 425

Marco, O. and Alloin, D., 2000, A&A, 353, 465

Mirabel, I. F., Laurent, O., Sanders, D. B., Sauvage, M., Tagger, M., Charmandaris, V., Vigroux, L., Gallais, P., Cesarsky, C. and Block, D. L., 1999, A&A, 341, 667

Mihalas, D., 1978, Stellar Atmospheres, San Francisco: W. H. Freeman

Meisenheimer, K., Haas, M., Mller, S.A.H., Chini, R., Klaas, U. and Lemke, D., 2001, A&A, 372, 719

Natta A. and Panagia, 1984, ApJ, 287, 228

Nenkova, M., Ivezić, Ž. and Elitzur, M., 2000, ASP Conference Series, vol. 196, Proc.of Workshop on Dust, Disks and Regholits, April'99, Houston,TX

Nenkova, M., Ivezić, Ž. and Elitzur, M., 2001, ASP Conference Series, vol. 247, Proc.of Conference 'Spectroscopic Challenges of Photoionized Plasmas', Nov'00, Lexington,KY

Nenkova, M., Ivezić, Ž. and Elitzur, M., 2002, ApJ, 570, L9

Norman C. et al, 2002, ApJ, 571, 218

Osterbrock, D. E. and Shaw, R.A., 1988, ApJ, 327, 89

Osterbrock, D. E., ApJ, 404, 551

Osterbrock, D. E. and Martel, A., 1993, ApJ, 414, 552

Peterson, B. M., 1997, Introduction to Active Galactic Nuclei, Cambridge Univ. Press

Pier, E., Krolik, J., 1992, ApJ, 401, 99

Pier, E., Krolik, J., 1993, ApJ, 418, 673

Polletta, M., Courvoisier, T. J.-L., Hooper, E.J. and Wilkes, B. J., 2000, A&A, 362, 75

Rieke, G. H. and Lebofsky, M. J., 1981, ApJ, 250, 87

Rieke and Low, 1975, ApJ, 199, L13

Robson, I., 1996, Active Galactic Nuclei, John Wiley and Sons, Ltd. in assoc. with Praxis Publishing, Ltd.

Roche, P., Whitmore, B., Aitken, D. and Phillips, M., 1984, MNRAS, 207, 35

Roche,P., Aitken, D., Smith, D. and Ward, M., 1991, MNRAS, 248, 606 (Roch91)

Rowan-Robinson, M., 1977, ApJ, 213, 635

Rowan-Robinson, M., 1995, MNRAS 272, 737

Sanders, D., Phinney, E., Neugebauer, G., Soifer, B. and Matthews, K., 1989, ApJ, 347, 29

Simpson, C., Mulchaey, J., Wilson, A., Ward, M. and Alonso-Herrero, A., 1996, ApJ, 457, L19

Schmidt-Burgk, J., 1975, A&A, 40, 249

Smith, D.A. and Done, C., 1996, MNRAS, 280, 355

Spoon, H., Keane, J., Tielens A., Lutz, D., Moorwood, A. and Laurent, O., 2002, A&A, 385, 1022

Stern, D. et al, 2002, ApJ, 568, 71

Storchi-Bergmann T., Mulchaey, J. and Wilson, A., 1992, ApJ, 395, 73

Tacconi, L., Genzel R., Blietz, M., Cameron, M., Harris, A. and Madden S., 1994, ApJ, 426, L77

Tomono, D., Yoshiyuki D., Tomonori, U. and Tetsuo N., 2001, ApJ, 557, 637

Wilkes, B., 2001, NewAR, 45, 641

Wills, B., 1999, in Quasars and Cosmology, ASP Conf. Ser., vol.162, Ed. G. Ferland and J. Baldwin

Wilson, A. and Tzvetanov, Z. I., 1994, AJ, 107, 1227

Witt, A. N. and Gordon, K. D., 2000, ApJ, 528, 799

VITA

Maia M. Nenkova

Date and place of birth:

    July 30, 1961; Plovdiv, Bulgaria

Educational institutions attended and degrees awarded:

    — M.S., University of Kentucky, 2000

    — B.S., Sofia University, 1984

Professional positions held:

    — Part-time Faculty, Sheridan College, Ontario, Canada, 2001-2002

    — Teaching Assistant, University of Kentucky, USA, 1994-1997; 2000-2001

    — Research Assistant, University of Kentucky, USA, 1997-2000

    — Research Assistant, Sofia University, Bulgaria, 1989-1992

    — Physicist, Institute of Optics, Sofia, Bulgaria, 1984-1985

Scholastic and professional honors:

    — Outstanding Teaching Assistant award, nominated 2003

    — American Astronomical Society, member since 1999

    — UK Center for Computational Sciences fellowship, 1997-2000

    — Academic Excellence Tuition Scholarship, UK, 1997-1998

Publications:

    — Nenkova, M., Ivezić, Ž. and Elitzur, M., 'Modeling AGN clumpy tori: support for the Unified Model', to be submitted in MNRAS

    — Nenkova, M., Ivezić, Ž. and Elitzur, M.,'Dust emission from AGN', 2002, ApJ, 70, L9

    — Nenkova, M., Elitzur, M. and Ivezić, Ž., 'Modeling AGN dust distributions with the continuum radiative transfer code DUSTY', in ASP Conference Series, vol. 247, 2001

    — Nenkova, M., Ivezić, Ž. and Elitzur, M., 'DUSTY: A publicly available

code for modeling dust emission', in ASP Conference Series, vol. 196, 2000

— Nenkova M. and Christopher, J., 'Active learning in the introductory calculus-based physics course at the University of Kentucky: results', presented at a meeting of the KAS/KAPT, Nov.15, 1997

— Baleva, M., Bozukov, L. and Momtchilova, M. , 'Phonons in polymorphous PbTe films on KCl substrates: I. IR reflectivity', 1992, J.Phys: Cond. Matter, 4, 4633

— Baleva, M., Ivanov, I. and Momtchilova, M., 'Phonons in polymorphous PbTe films on KCl substrates: II. IR and Raman spectra', 1992, J.Phys: Cond. Matter, 4, 4645

— Baleva, M., Mateeva, M. and Momtchilova, M., 'Direct energy gaps in PbTe high-pressure phases and energies of the heterophase junctions', 1992, J.Phys: Cond. Matter, 4, 8997

User Manual:

— Ivezić, Ž., Nenkova, M. and Elitzur, M. 1999, User Manual for DUSTY, Internal Report, Univ. of Kentucky, *http://www.pa.uky.edu/∼moshe/dusty*

Maia Nenkova

May 8, 2003